

ADVANCED MATERIALS

Supporting Information

for *Adv. Mater.*, DOI 10.1002/adma.202415774

Programmable Magnetic Hysteresis in Orthogonally-Twisted 2D CrSBr Magnets via Stacking Engineering.

Carla Boix-Constant, Andrey Rybakov, Clara Miranda-Pérez, Gabriel Martínez-Carracedo, Jaime Ferrer, Samuel Mañas-Valero and Eugenio Coronado**

Supporting information for**Programmable Magnetic Hysteresis in Orthogonally-Twisted Two-Dimensional CrSBr Magnets via Stacking Engineering.**

Carla Boix-Constant, Andrey Rybakov, Clara Miranda-Pérez, Gabriel Martínez-Carracedo, Jaime Ferrer, Samuel Mañas-Valero, Eugenio Coronado**

C. Boix-Constant, A. Rybakov, C. Miranda-Pérez, E. Coronado

Instituto de Ciencia Molecular (ICMol), Universitat de València, Catedrático José Beltrán 2, Paterna, 46980 Spain.

E-mail: eugenio.coronado@uv.es

G. Martínez-Carracedo, J. Ferrer

Departamento de Física, Universidad de Oviedo, 33007 Oviedo, Spain.

Centro de Investigación en Nanomateriales y Nanotecnología, Universidad de Oviedo-CSIC, 33940 El Entrego, Spain.

S. Mañas-Valero

Department of Quantum Nanoscience, Kavli Institute of Nanoscience, Delft University of Technology, Delft 2628CJ, The Netherlands.

E-mail: S.ManasValero@tudelft.nl

Contents

1.- Summary of the fabricated devices.....	2
1.1.- Angular field dependence	4
1.2.- Temperature dependence	7
1.3.- Temperature dependence for different in-plane magnetic fields.....	10
2.- First-order reversal curves.....	13
2.1.- Angular dependence (initial saturation at negative fields)	13
2.2.- Angular dependence (initial saturation at positive fields)	17
2.3.- Temperature dependence	21
3.- Micromagnetic simulations.....	23
4.- Simplified model of the spin-switching process for orthogonally-twisted CrSBr.....	31
5. References	34

1.- Summary of the fabricated devices.

A total of 11 devices are considered in this work (denoted as MM, MB and BB in the **Table S1**, which corresponds to monolayer/monolayer, monolayer/bilayer and bilayer/bilayer, respectively). Devices MM1, MM2 and MM3 correspond to device 2, 3 and 1 from our previous work [1], where MM1 and MM2 are fabricated with few-layers graphene as contacts and MM3 with NbSe₂ as contacts. MB and BB devices are fabricated with few-layers graphene contacts. Although the exact details vary from device to device, probably due to slight field misalignments or fabrication imperfections in the twist angle or strain of the layers, the overall phenomenology is robust and consistent among devices.

Table S1.- Summary of the fabricated devices.

Device	Bottom layer		Top layer		Overlap area (μm^2)	Twist angle (°)
	Number of layers	Area (μm^2)	Number of layers	Area (μm^2)		
MM1	1	117.3	1	190.1	15.9	89.3
MM2	1	206.6	1	121.1	7.9	87.0
MM3	1	53.3	1	77.2	9.3	92.5
MB1	2	73.8	1	64.6	8.9	91.7
MB2	2	86.5	1	70.0	6.4	89.8
MB3	2	146.2	1	376.2	7.7	91.3
MB4	2	113.6	1	285.5	17.0	87.8
BB1	2	123.7	2	179.5	11.8	86.2
BB2	2	209.3	2	166.7	8.9	86.4
BB3	2	86.5	2	150.6	3.7	89.1
BB4	2	113.6	2	285.5	17.0	87.8

In general trends, the three cases of orthogonally-twisted heterostructures exhibit common trends: starting at -3 T and sweeping towards positive magnetic fields (red trace in the **Figure S1**), the resistance exhibits its minimum value and remains constant up to -1 T. Thus, in accordance with a spin-valve picture, the layers' magnetization is parallel and aligned along the applied magnetic field, being the magneto-resistance (MR) zero (MR is defined as

$100 \cdot [R(B) - R(P)]/R(P)$, where $R(P)$ is the resistance when the magnetization of all the layers is parallel; in our case, we consider the resistance value at 3 T). Below -1 T —field needed for reorienting the spins from the easy to the intermediate magnetic axis in a single layer of CrSBr—, the resistance increases as a consequence of the canting of the top layer towards its own easy-magnetic axis and reaches a maximum near zero-field (in particular, at +40 mT with $MR = 4\%$, +190 mT with $MR = 25\%$ and -20 mT with $MR = 44\%$ for the monolayer/monolayer, monolayer/bilayer and bilayer/bilayer case, respectively), when the spin-flip of the bottom layer occurs. Upon further increasing the field, the resistance decreases again (canting of the top layer towards the applied field) up to +1 T, when it finally saturates. Sweeping the field from positive to negative fields (blue trace in the **Figure S1**) yields to a symmetric curve, characterized by the appearance of magnetic hysteresis. The hysteresis can be better visualized by computing the increment, ΔX , defined as $\Delta X = X_{+B \rightarrow -B} - X_{-B \rightarrow +B}$ (X indicates either the R or the MR), being non-zero ΔX values hysteretic regions (yellow trace in the **Figure S1**). Note that the appearance of hysteresis contrast with the pristine monolayer and bilayer CrSBr, where no significant hysteresis is observed.^[2,3]

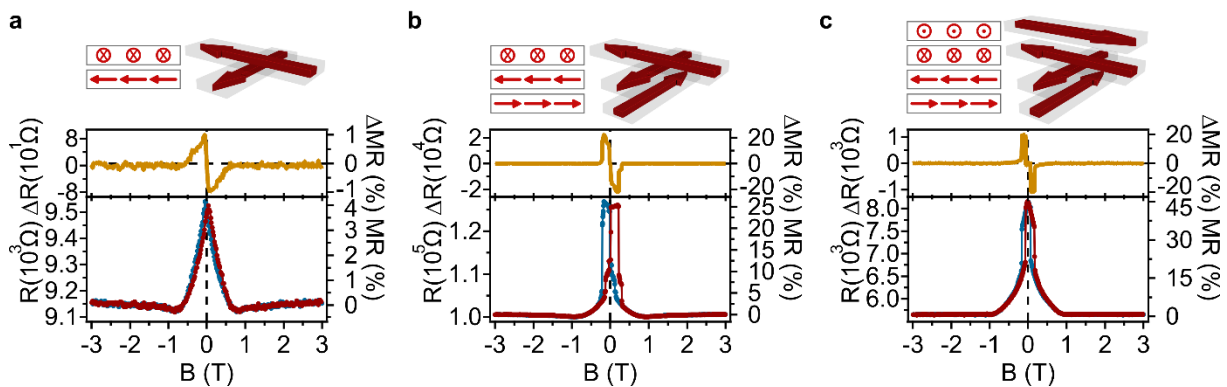


Figure S1.- Magneto-resistance properties of orthogonally-twisted monolayer/monolayer, monolayer/bilayer and bilayer/bilayer CrSBr. a-c) Field dependence of the resistance (R), the magneto-resistance (MR) and its increment (Δ), defined as $\Delta X = X_{+B \rightarrow -B} - X_{-B \rightarrow +B}$ (X indicates either the R or the MR) for a) monolayer/monolayer, b) monolayer/bilayer and c) bilayer/bilayer orthogonally-twisted CrSBr at $T = 2$ K and $\theta = 90^\circ$, as sketched in Figure 1. Sweeping up (down) trace is denoted in red (blue). MR is defined as $MR (\%) = 100 \cdot [R(B) - R(P)]/R(P)$, where $R(P)$ is the resistance in the parallel state (in this case, at 3 T).

1.1.- Angular field dependence.

In this section, the angular in-plane field dependence of the resistance as well as the resistance increment for all the devices is presented at T = 2 K.

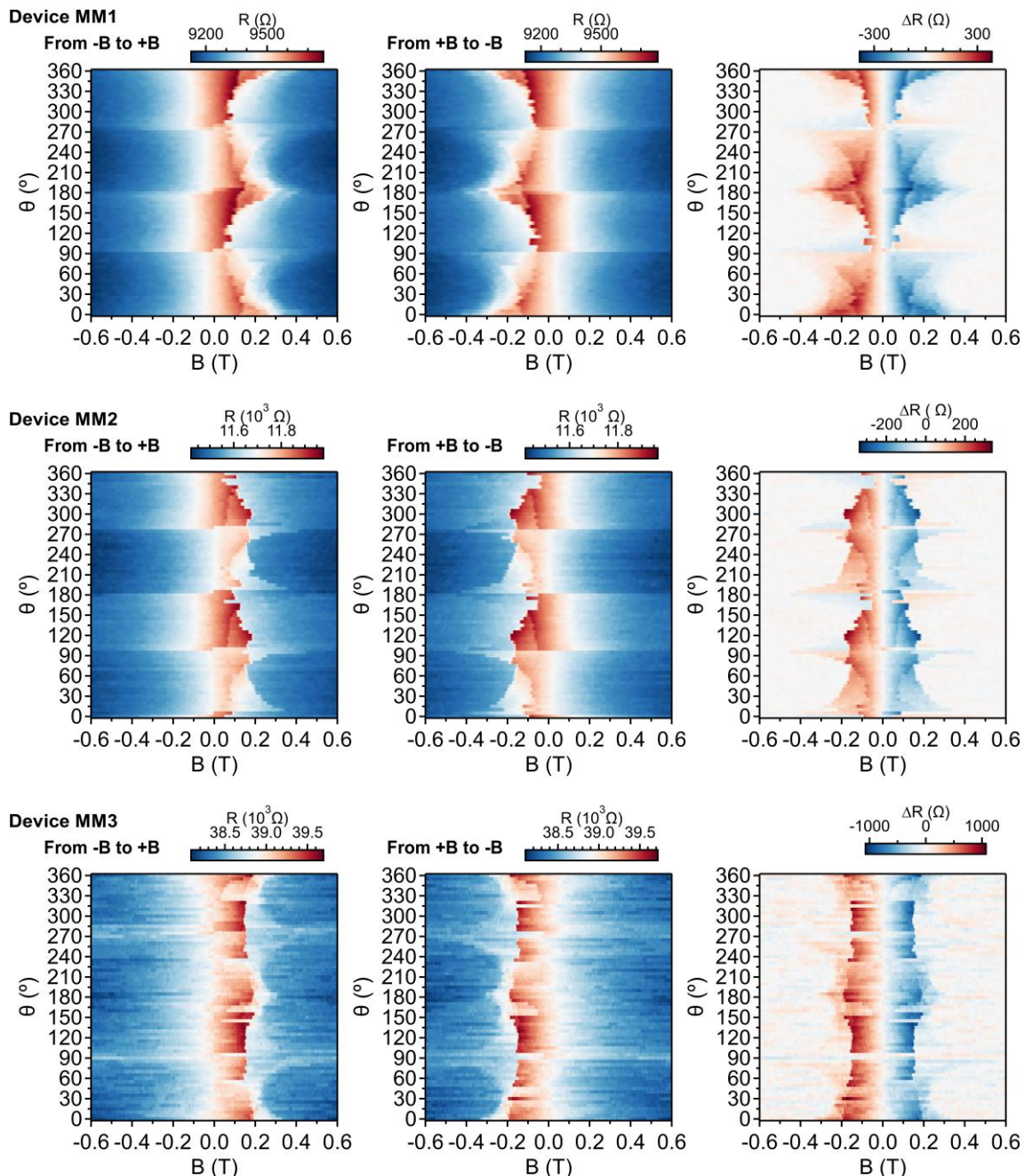


Figure S2.- Angular in-plane field dependence for orthogonally-twisted monolayer/monolayer CrSBr at 2K. Left panel) Resistance while switching the field from negative to positive values. Middle panel) Resistance while switching the field from positive to negative values. Right panel) Resistance increment ($\Delta R = R_{+B \rightarrow -B} - R_{-B \rightarrow +B}$). Non-zero regions (that is, red and blue areas) correspond to hysteretic areas.

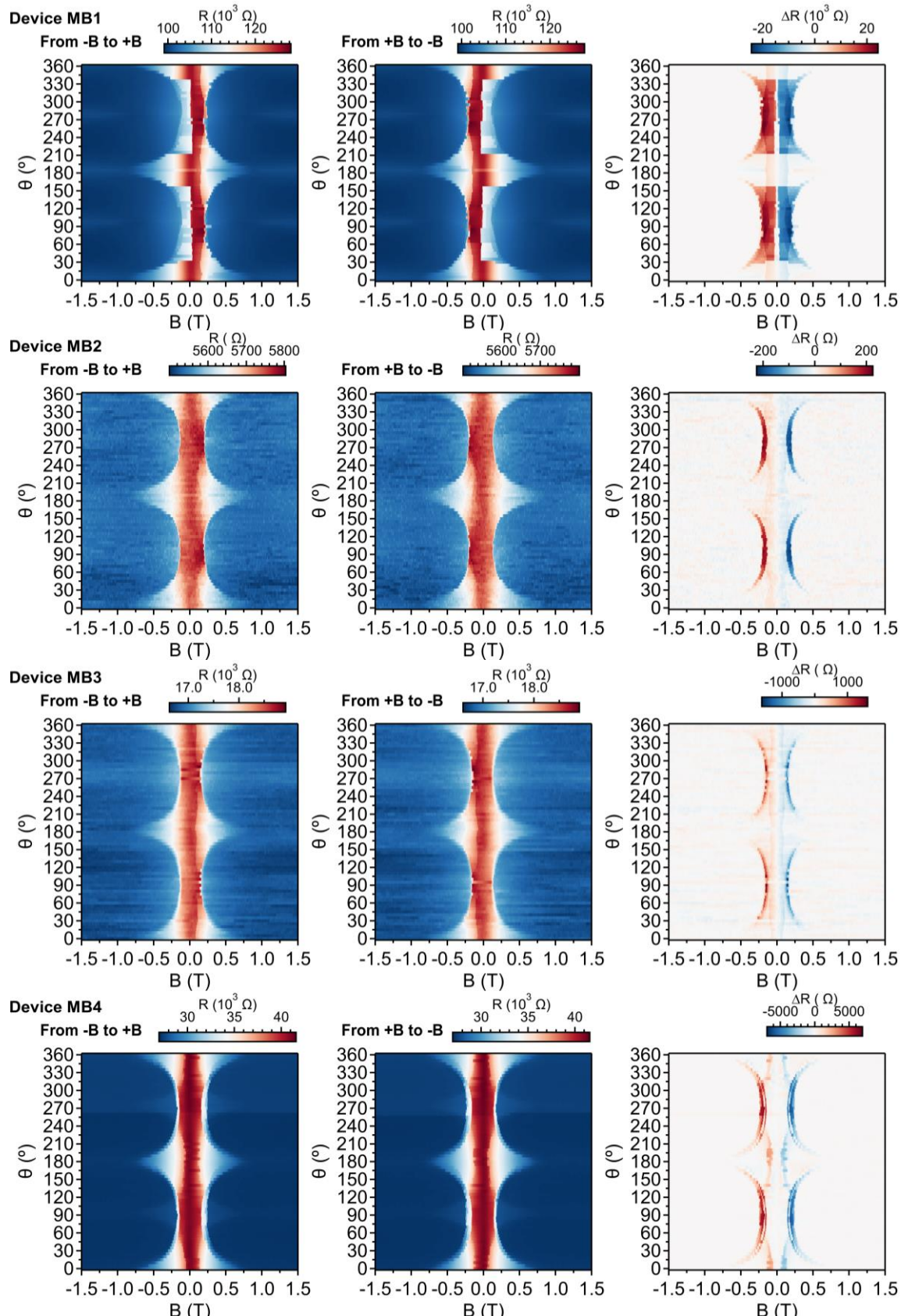


Figure S3.- Angular in-plane field dependence for orthogonally-twisted monolayer/bilayer CrSBr at 2K. Left panel) Resistance while switching the field from negative to positive values. Middle panel) Resistance while switching the field from positive to negative values. Right panel) Resistance increment ($\Delta R = R_{+B \rightarrow -B} - R_{-B \rightarrow +B}$). Non-zero regions (that is, red and blue areas) correspond to hysteretic areas.

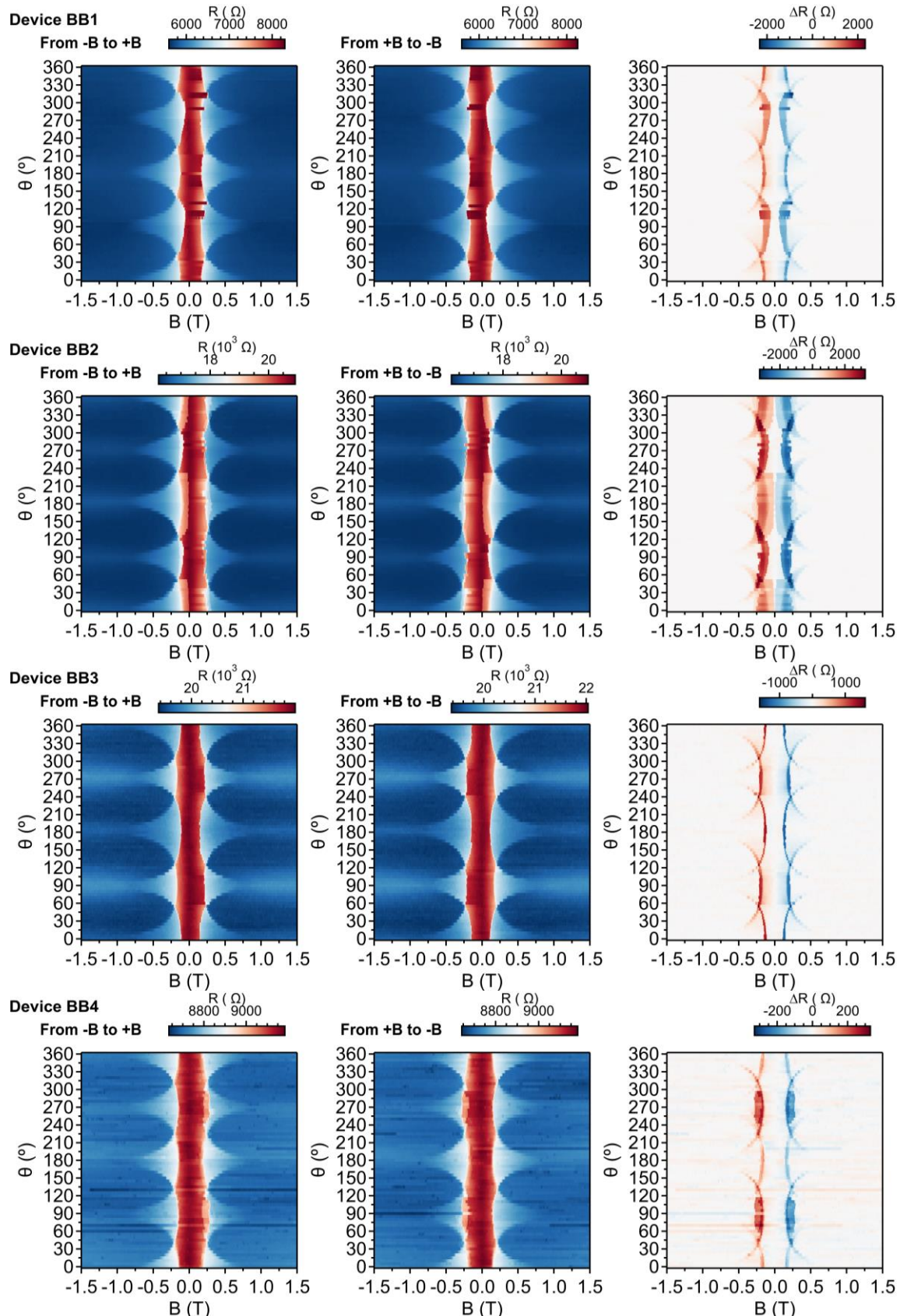


Figure S4.- Angular in-plane field dependence for orthogonally-twisted bilayer/bilayer CrSBr at 2K. Left panel) Resistance while switching the field from negative to positive values. Middle panel) Resistance while switching the field from positive to negative values. Right panel) Resistance increment ($\Delta R = R_{+B \rightarrow -B} - R_{-B \rightarrow +B}$). Non-zero regions (that is, red and blue areas) correspond to hysteretic areas.

1.2.- Temperature dependence.

In this section, the temperature and field dependence of the resistance as well as the resistance increment for all the devices is presented at $\theta = 90^\circ$.

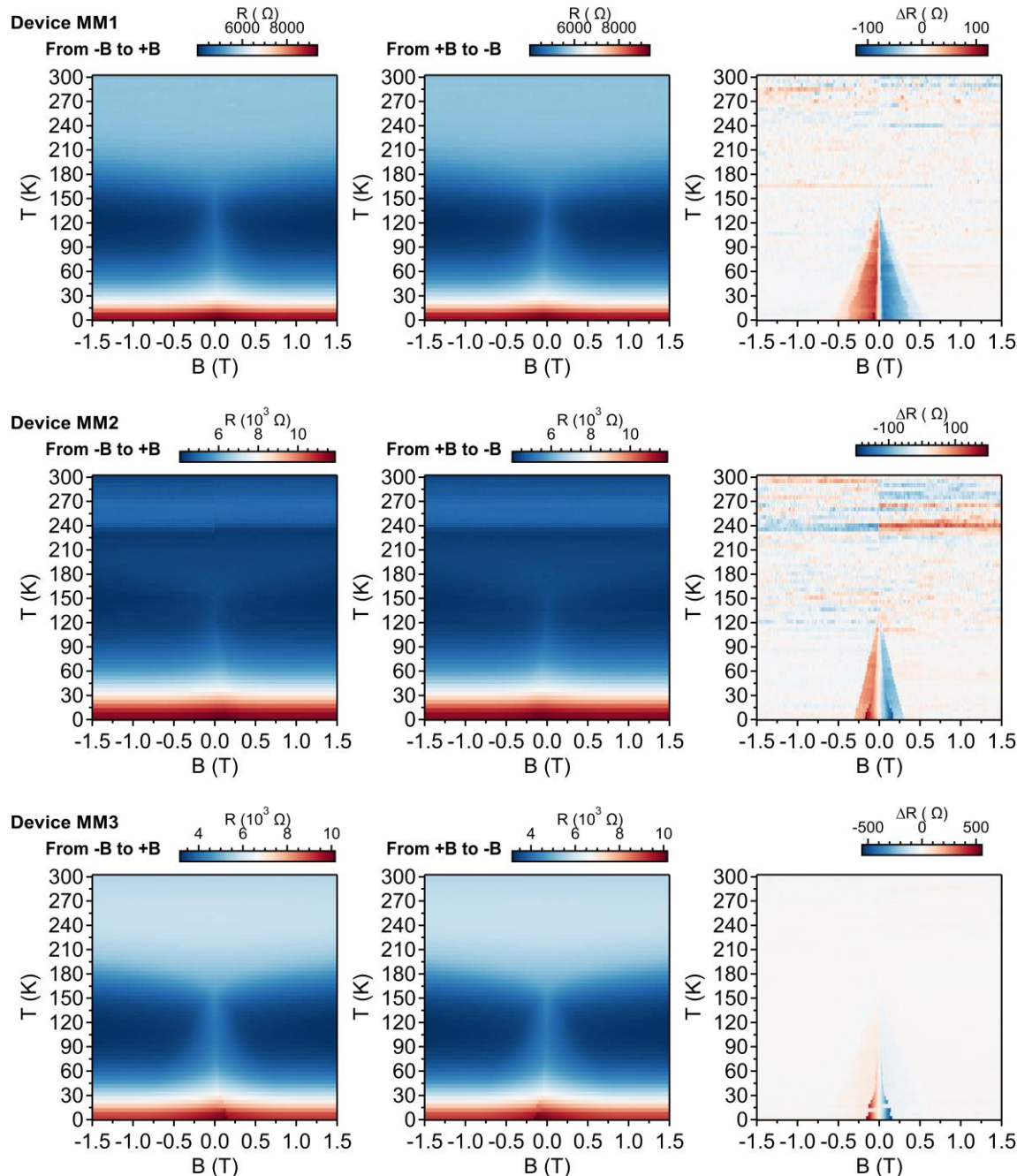


Figure S5.- Temperature and field dependence for orthogonally-twisted monolayer/monolayer CrSBr at $\theta = 90^\circ$. Left panel) Resistance while switching the field from negative to positive values. Middle panel) Resistance while switching the field from positive to negative values. Right panel) Resistance increment ($\Delta R = R_{+B \rightarrow -B} - R_{-B \rightarrow +B}$). Non-zero regions (that is, red and blue areas) correspond to hysteretic areas.

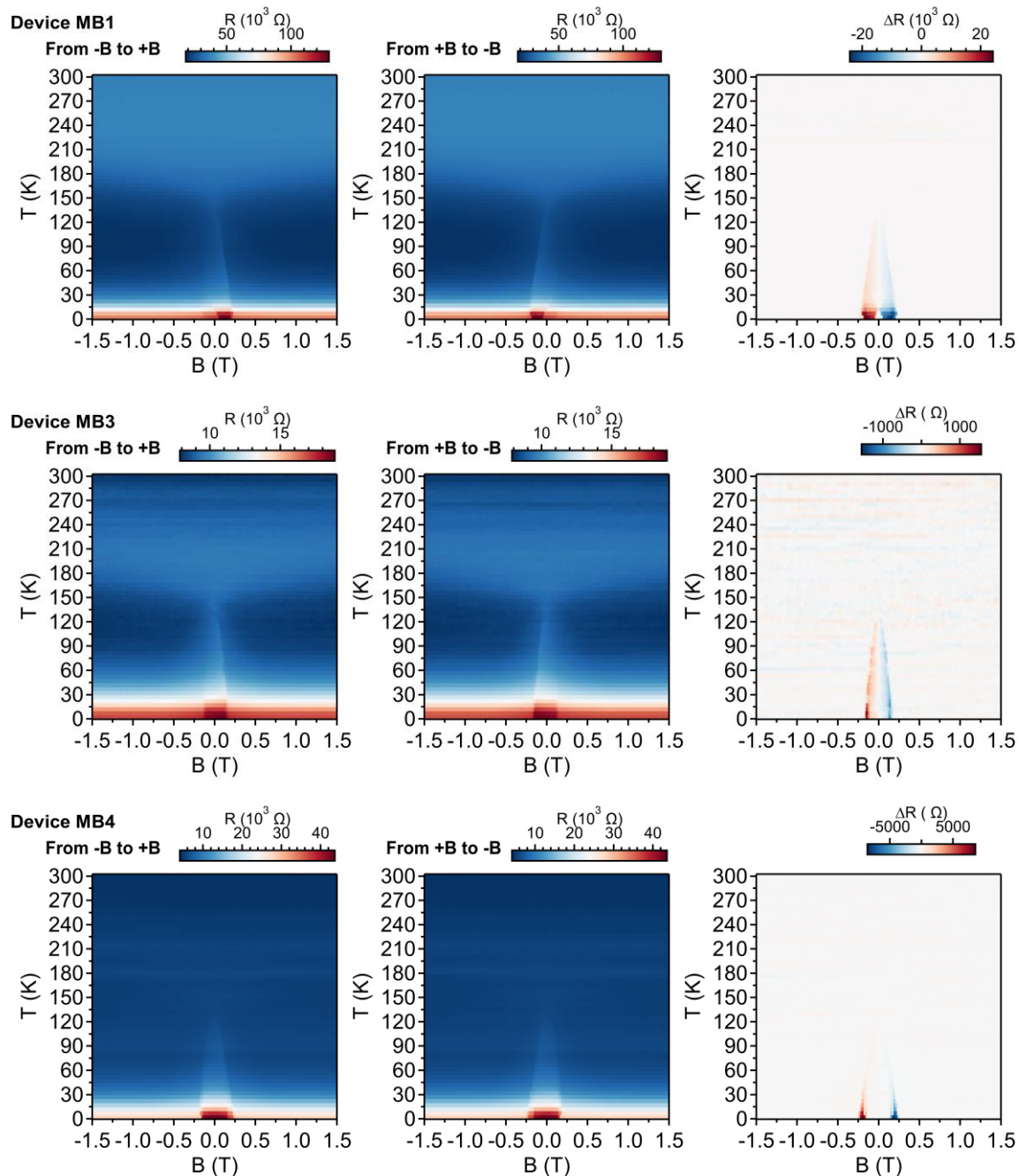


Figure S6.- Temperature and field dependence for orthogonally-twisted monolayer/bilayer CrSBr at $\theta = 90^\circ$. Left panel) Resistance while switching the field from negative to positive values. Middle panel) Resistance while switching the field from positive to negative values. Right panel) Resistance increment ($\Delta R = R_{+B \rightarrow -B} - R_{-B \rightarrow +B}$). Non-zero regions (that is, red and blue areas) correspond to hysteretic areas.

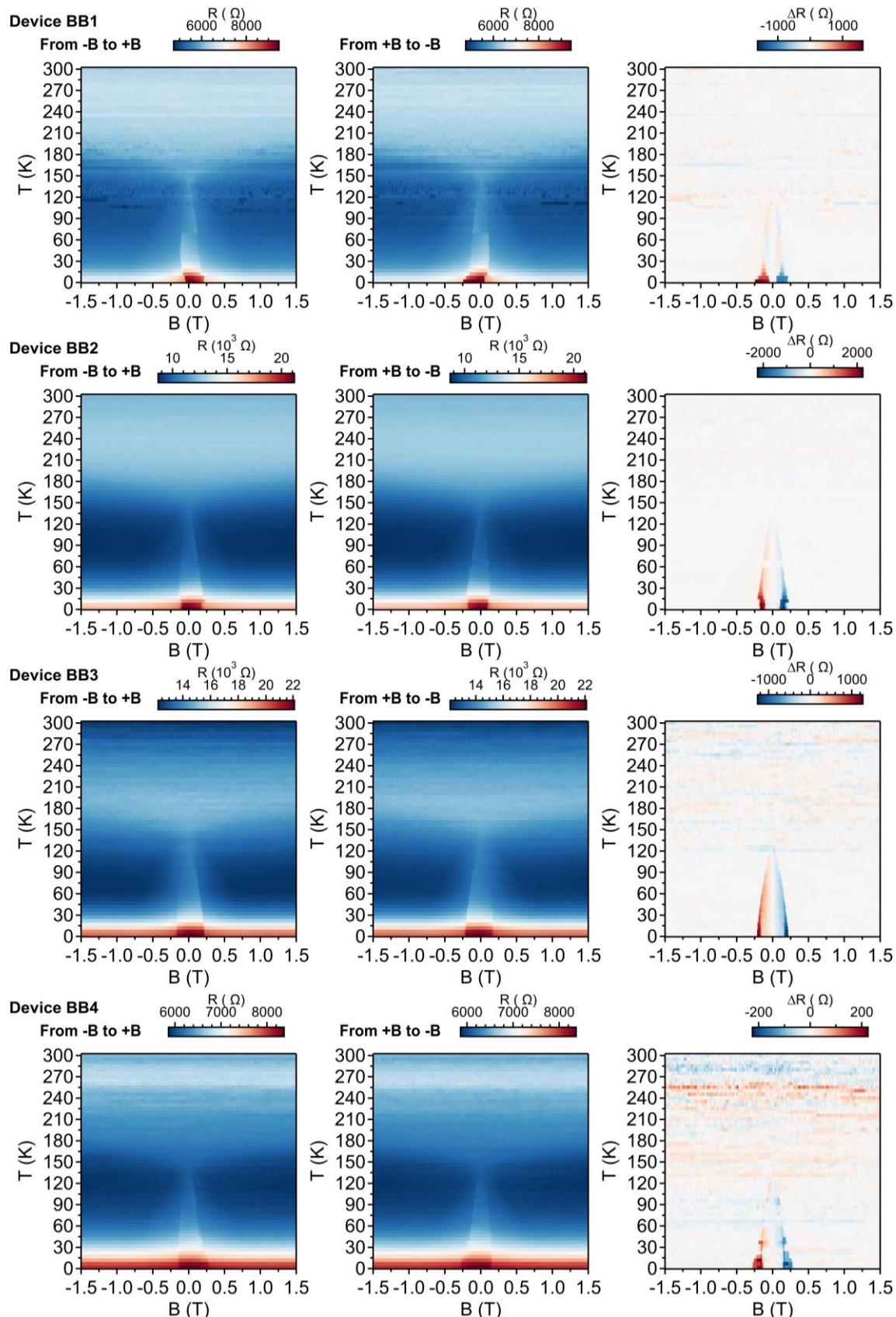


Figure S7.- Temperature and field dependence for orthogonally-twisted bilayer/bilayer CrSBr at $\theta = 90^\circ$. Left panel) Resistance while switching the field from negative to positive values. Middle panel) Resistance while switching the field from positive to negative values. Right panel) Resistance increment ($\Delta R = R_{+B \rightarrow -B} - R_{-B \rightarrow +B}$). Non-zero regions (that is, red and blue areas) correspond to hysteretic areas.

1.3.- Temperature dependence for different in-plane magnetic fields.

In this section, we show the thermal and field dependence of the resistance for representative devices upon different in-plane field orientations.

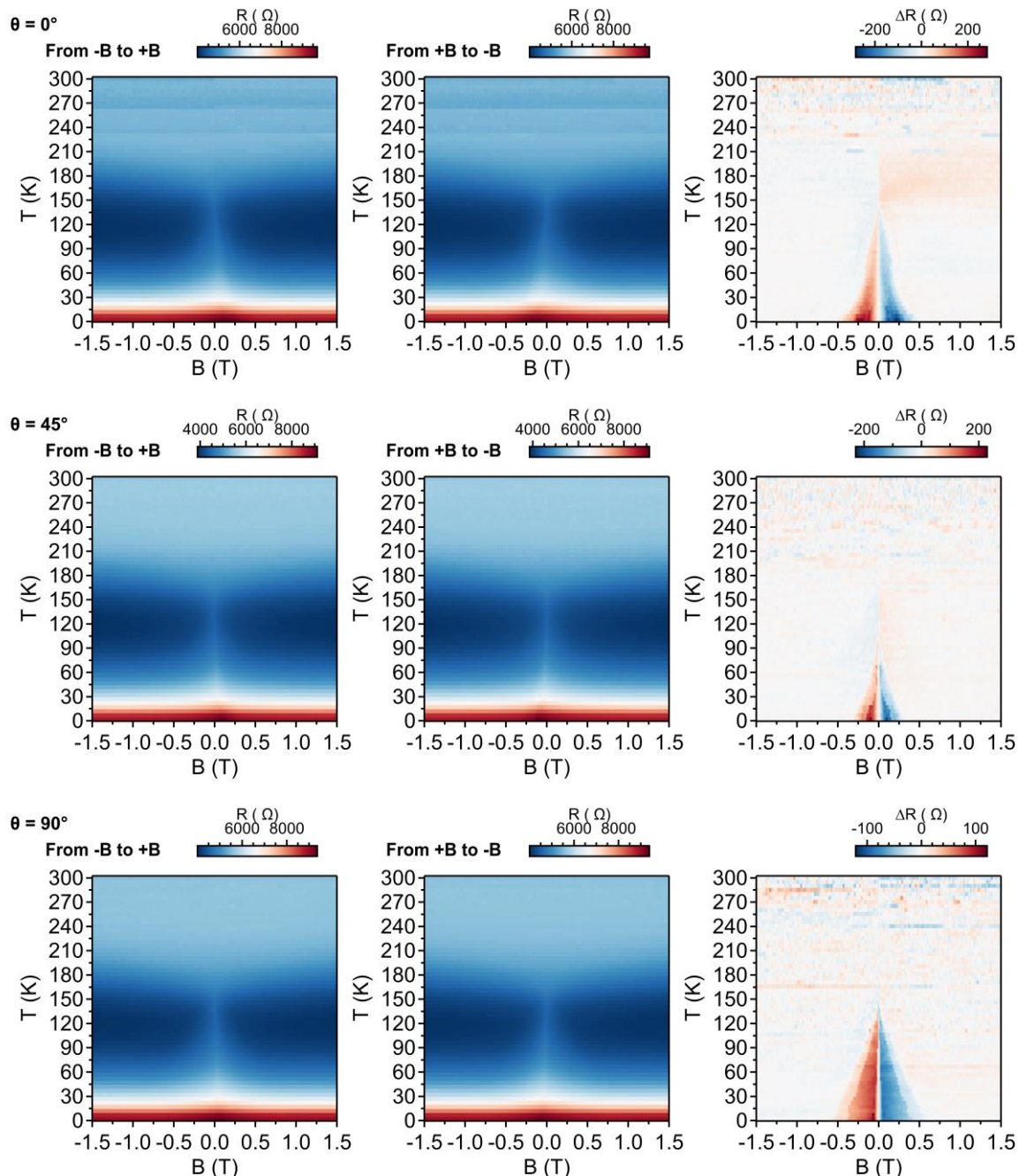


Figure S8.- Temperature and field dependence for orthogonally-twisted bilayer/bilayer CrSBr at different in-plane magnetic field directions for device MM1. Left panel) Resistance while switching the field from negative to positive values. Middle panel) Resistance while switching the field from positive to negative values. Right panel) Resistance increment ($\Delta R = R_{+B \rightarrow -B} - R_{-B \rightarrow +B}$). Non-zero regions (that is, red and blue areas) correspond to hysteretic areas.

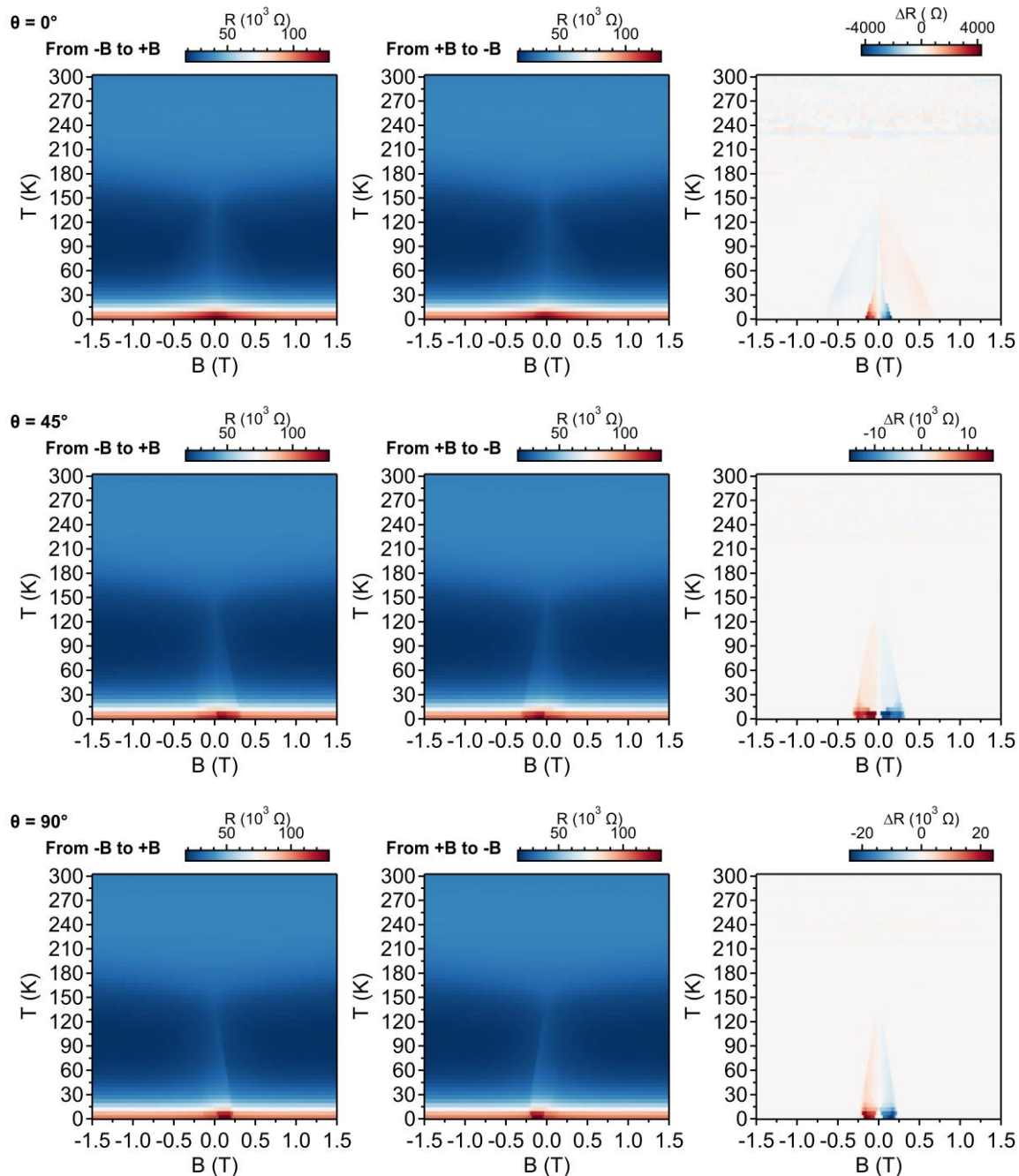


Figure S9.- Temperature and field dependence for orthogonally-twisted bilayer/bilayer CrSBr at different in-plane magnetic field directions for device MB1. Left panel) Resistance while switching the field from negative to positive values. Middle panel) Resistance while switching the field from positive to negative values. Right panel) Resistance increment ($\Delta R = R_{+B \rightarrow -B} - R_{-B \rightarrow +B}$). Non-zero regions (that is, red and blue areas) correspond to hysteretic areas.

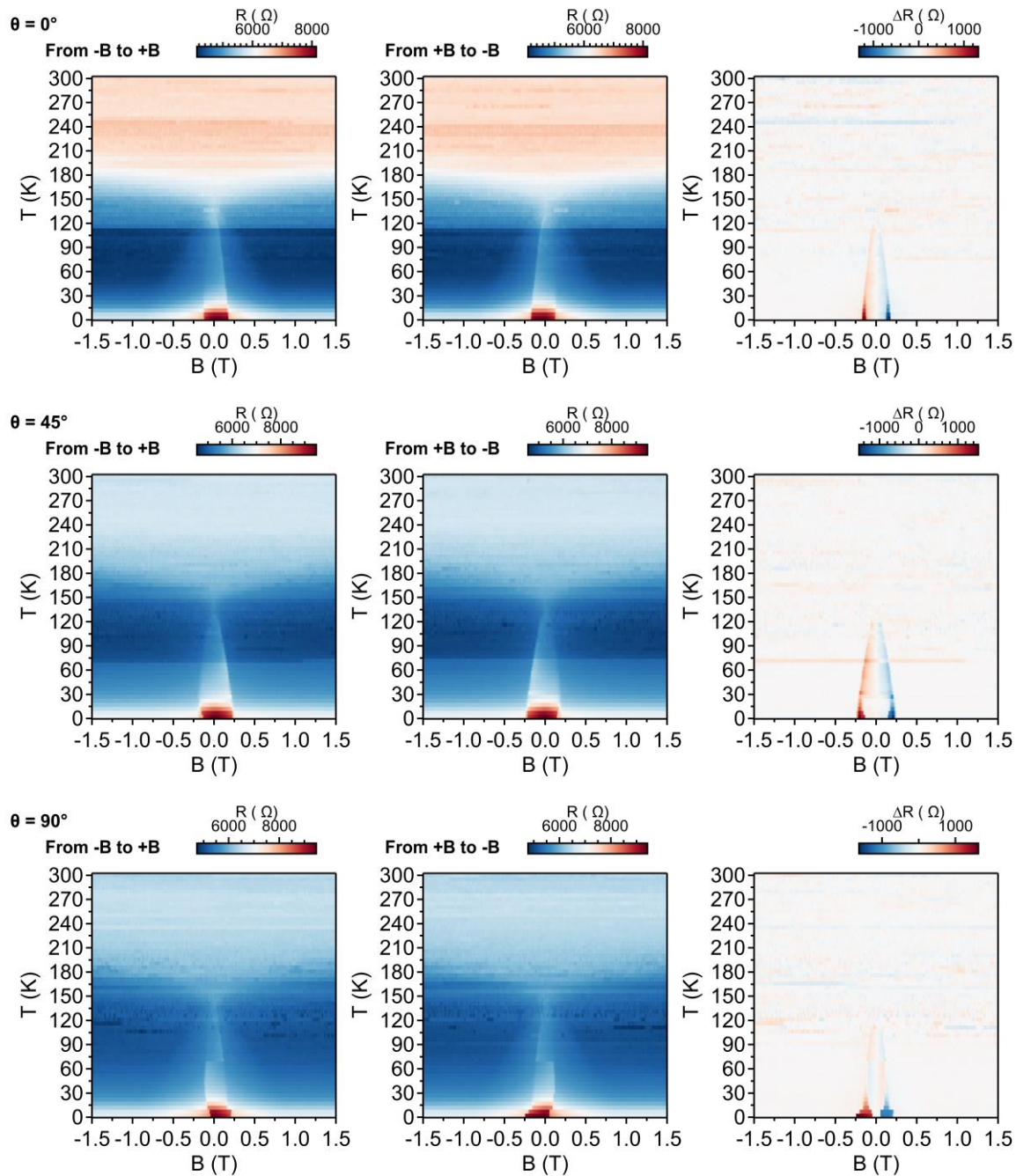
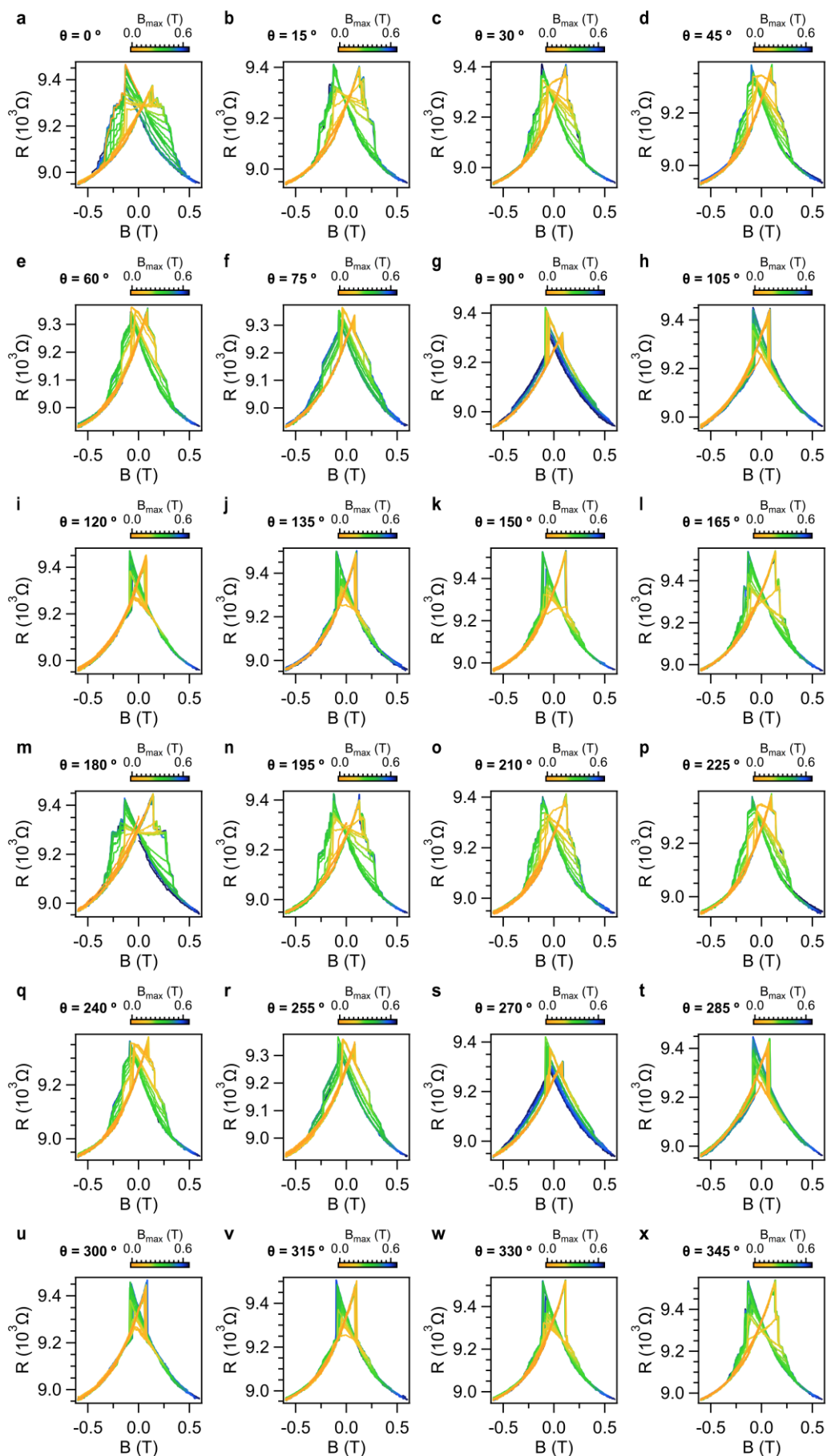


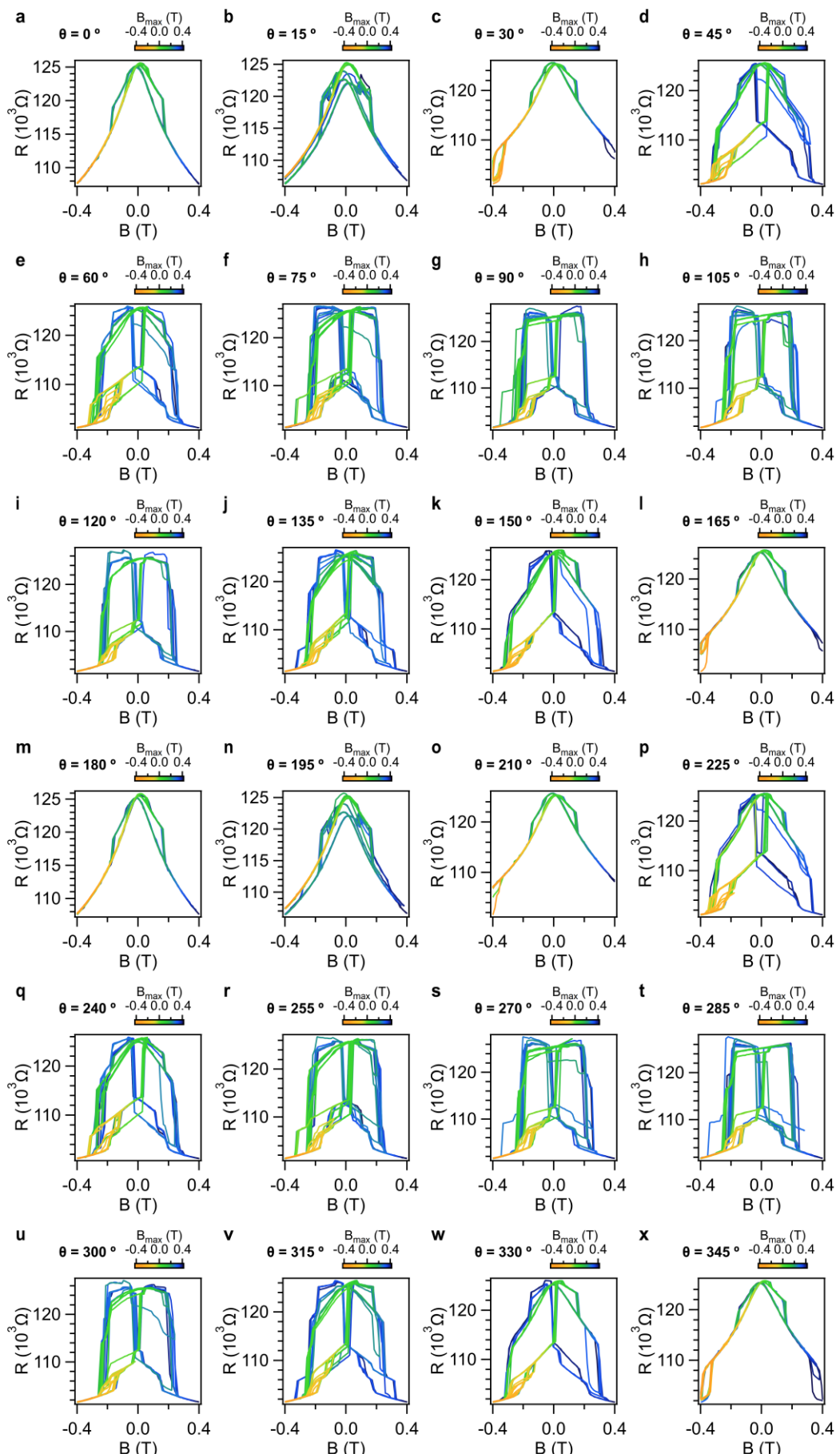
Figure S10.- Temperature and field dependence for orthogonally-twisted bilayer/bilayer CrSBr at different in-plane magnetic field directions for device BB1. Left panel) Resistance while switching the field from negative to positive values. Middle panel) Resistance while switching the field from positive to negative values. Right panel) Resistance increment ($\Delta R = R_{+B \rightarrow -B} - R_{-B \rightarrow +B}$). Non-zero regions (that is, red and blue areas) correspond to hysteretic areas.

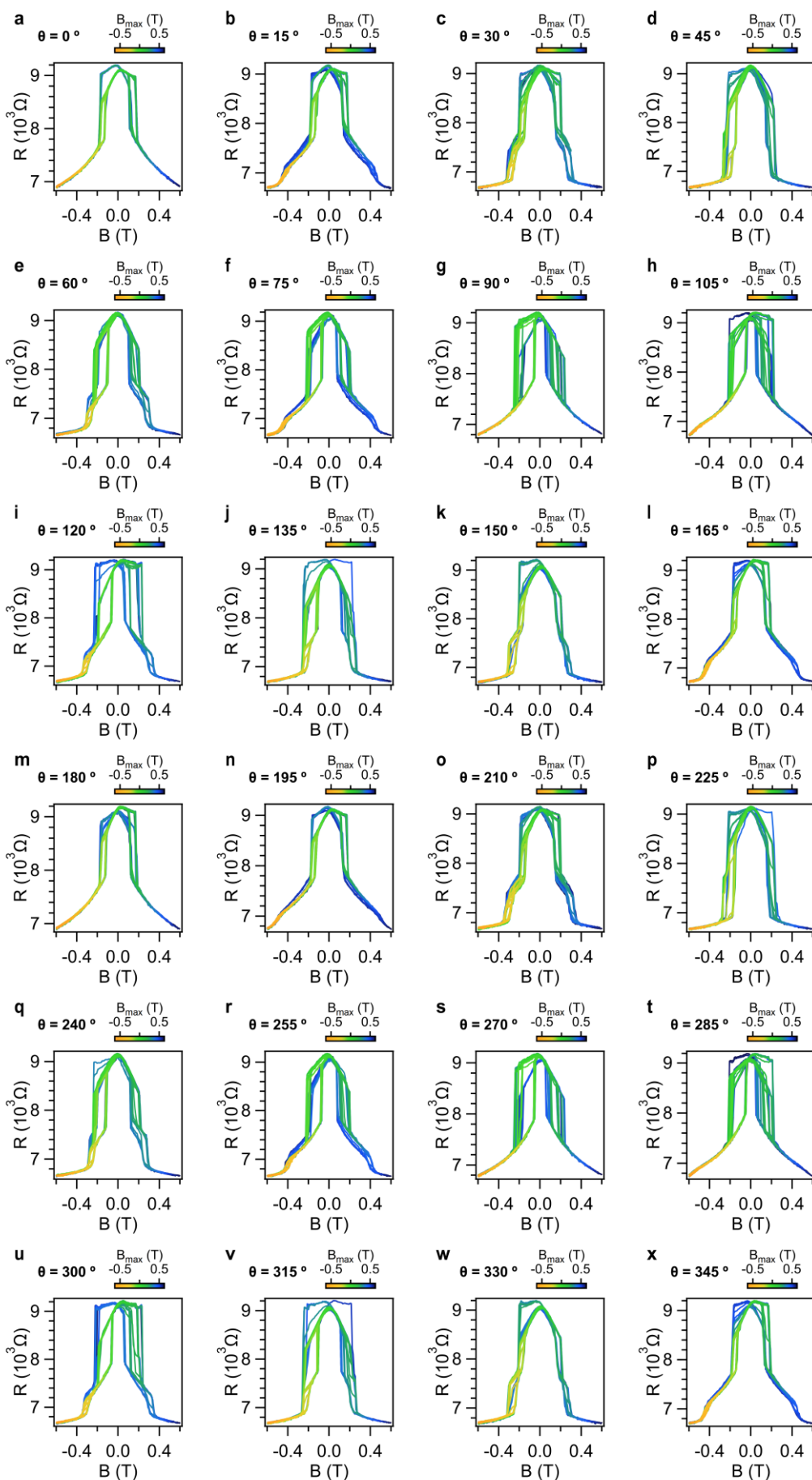
2.- First-order reversal curves.

2.1.- Angular dependence (initial saturation at negative fields).

In this section, we show the first order reversal curves for representative devices at $T = 2\text{ K}$ and different in-plane field orientations. After saturating at -3 T , we consider the sequence $-0.6\text{ T} \rightarrow B_{\max} \rightarrow -0.6\text{ T}$. In every field sweep, B_{\max} is incremented in steps of 20 mT .

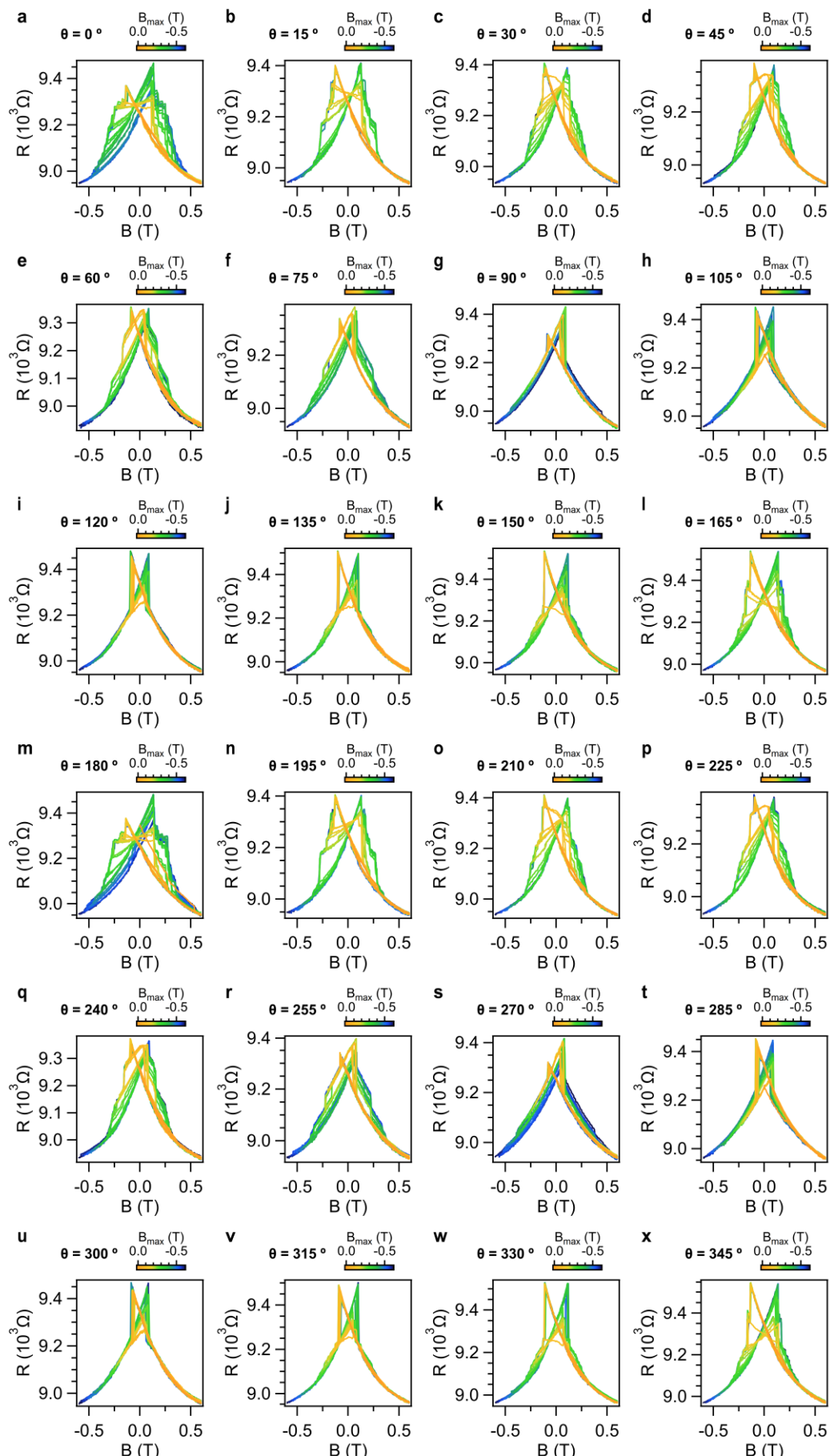
**Figure S11.-** First-order reversal curve (device MM1).

**Figure S12.-** First-order reversal curve (device MB1).

**Figure S13.-** First-order reversal curve (device BB1).

2.2.- Angular dependence (initial saturation at positive fields).

In this section, we show the first order reversal curves for representative devices at $T = 2\text{ K}$ and different in-plane field orientations. After saturating at $+3\text{ T}$, we consider the sequence $+0.6\text{ T} \rightarrow B_{\max} \rightarrow +0.6\text{ T}$. In every field sweep, B_{\max} is incremented in steps of 20 mT .

**Figure S14.-** First-order reversal curve (device MM1).

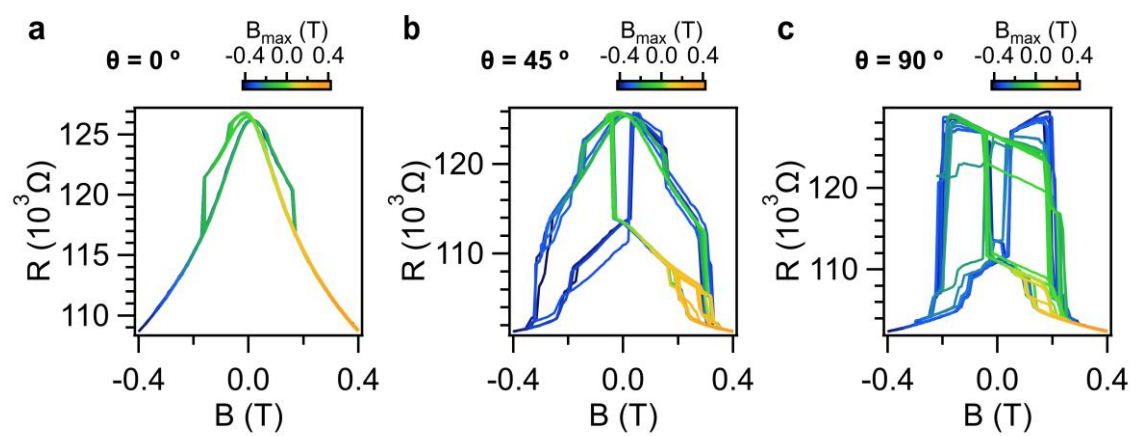
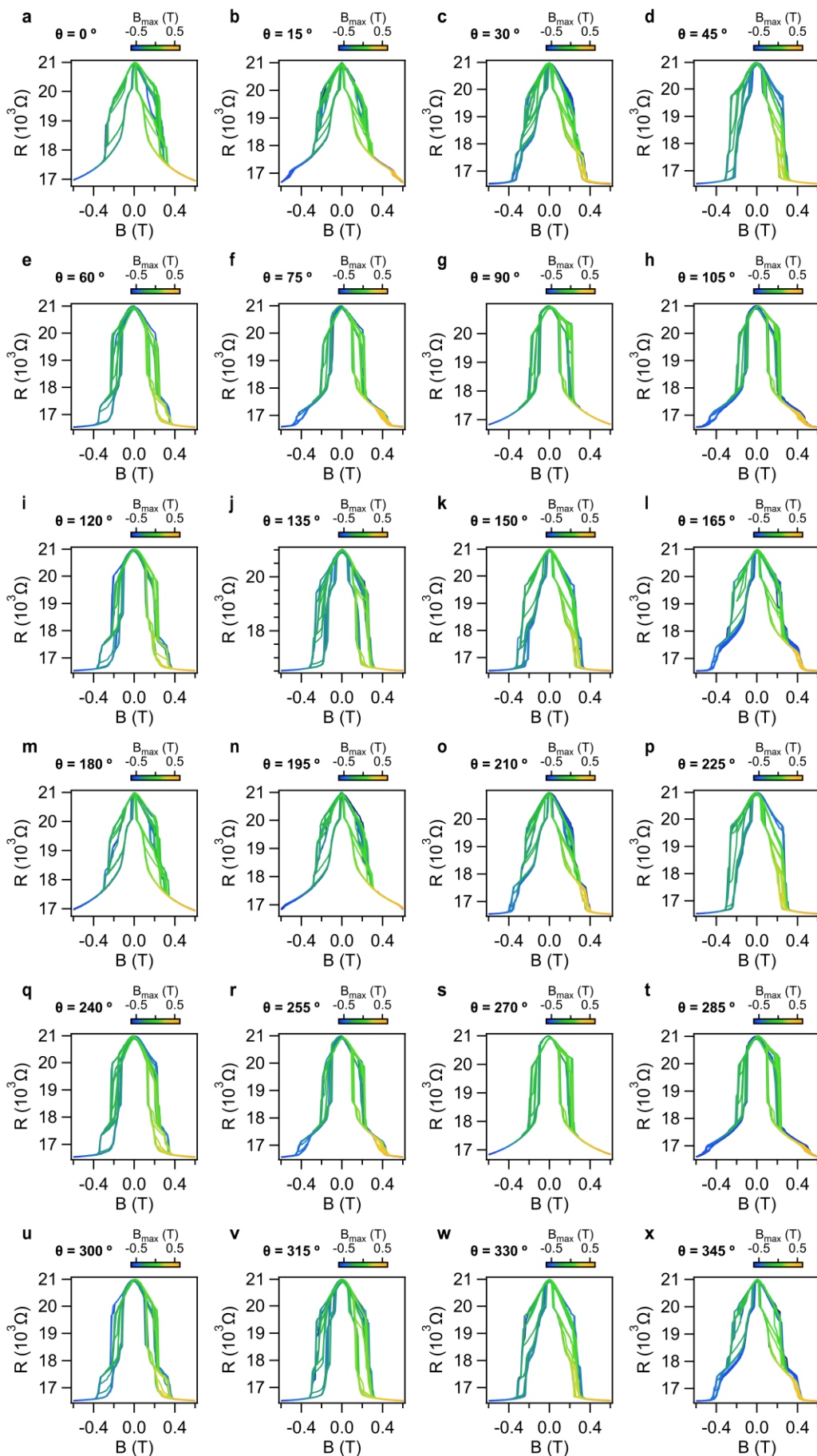


Figure S15.- First-order reversal curve (device MB1).



2.3.- Temperature dependence.

In this section, we show the first order reversal curves for representative devices at different temperatures and in-plane field orientations. After saturating at -3 T, we consider the sequence $-0.6 \text{ T} \rightarrow B_{\max} \rightarrow -0.6 \text{ T}$. In every field sweep, B_{\max} is incremented in steps of 20 mT.

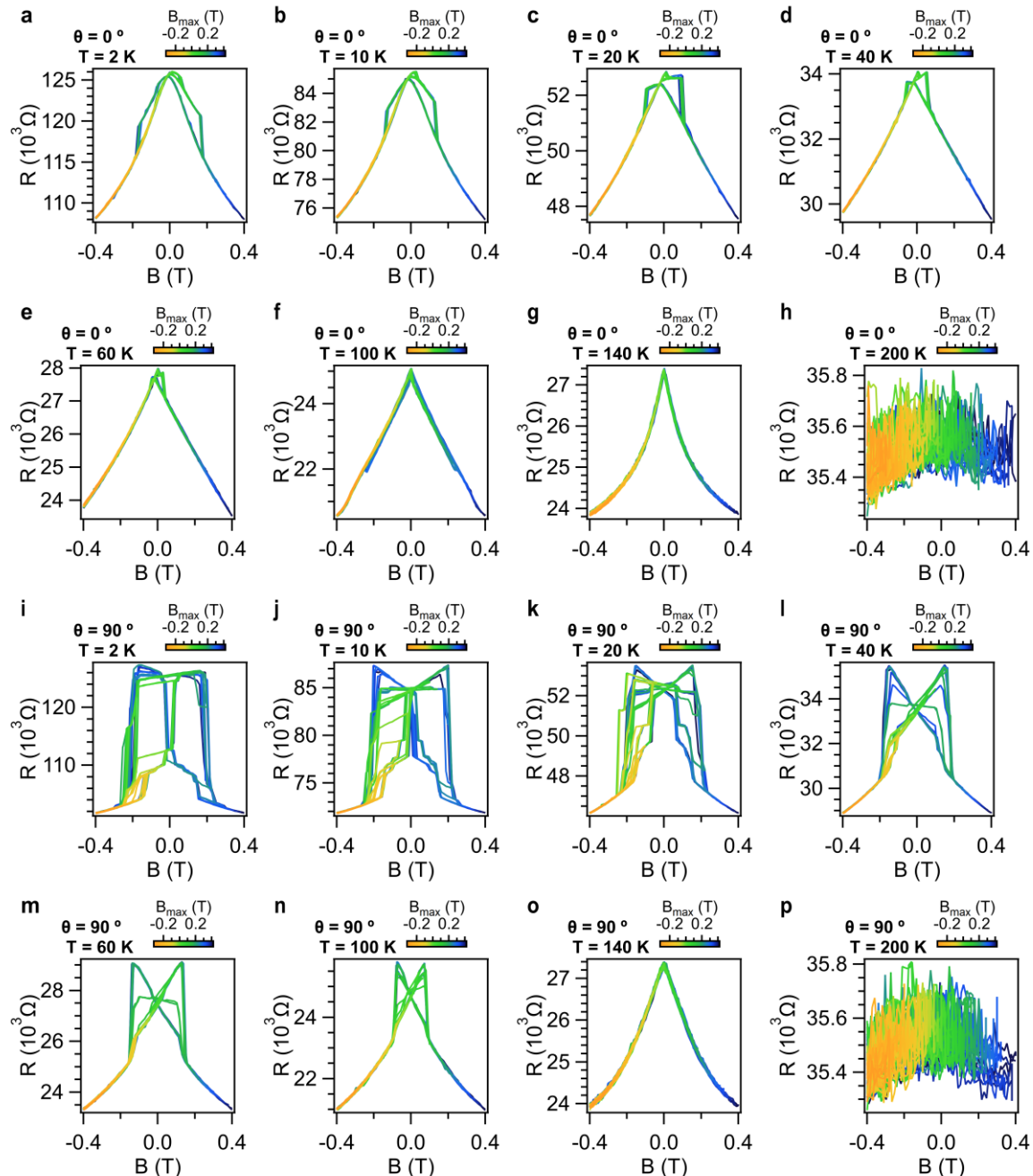


Figure S17.- First-order reversal curve (device MB1).

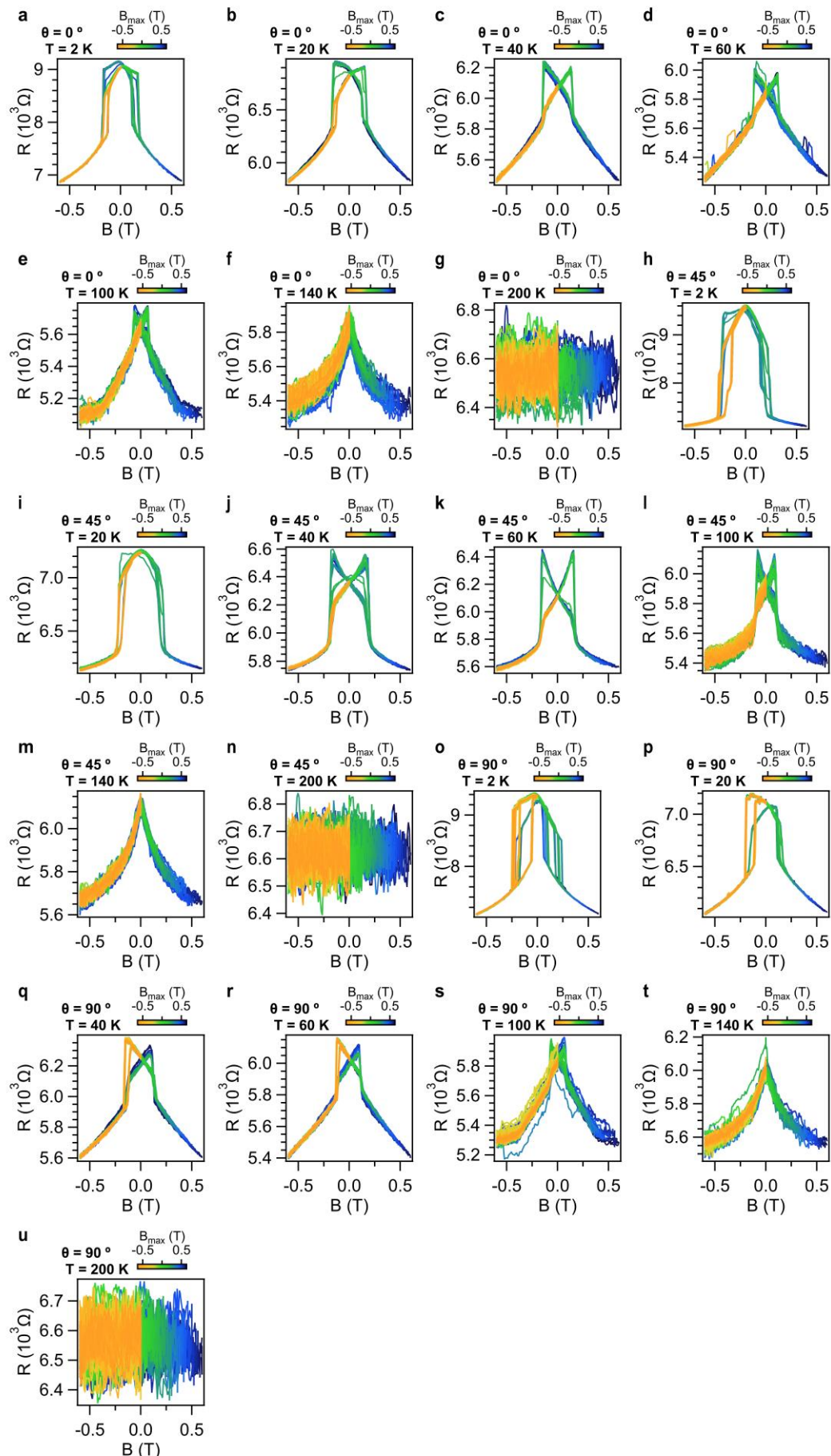


Figure S18.- First-order reversal curve (device BB1).

3.- Micromagnetic simulations.

For DFT calculations of orthogonally twisted monolayer/monolayer we select a 4 by 3 unit cell along the *a* and *b* axes, respectively, using the optimized parameters for the twisted bilayer, where $4a=14.458 \text{ \AA}$ and $3b=14.457 \text{ \AA}$ at $U=J=0 \text{ eV}$. Atomic force relaxation was performed with a minimum tolerance equal to 0.01 eV/\AA . Atomistic magnetic exchange and on-site anisotropy parameters are obtained using GROGU code^[4] which is based on the torque-LKAG formalism^[5] generalized for non-orthogonal basis sets when relativistic effects coming from spin-orbit coupling (SOC) are present. Localized magnetic entities were projected onto the Cr 3d-orbitals for a correct mapping to the Heisenberg model. For the mapping on the Heisenberg model the values of $U=3\text{eV}$, $J=1\text{eV}$ were used.

For the micromagnetic simulations of pristine bilayer we create a square of the size of $1 \times 1 \text{ micrometer}^2$. For each orthogonally twisted system both twisted and untwisted parts have the size of $1.47 \times 1.47 \text{ micrometers}^2$. The twisted part of each device is shifted in plane in order to have both overlapped and freestanding regions in the simulations. The overlap area has the square shape of the size $0.93 \times 0.93 \text{ micrometers}^2$ (see **Figure 5a**).

For all simulated devices an ideal crystal is assumed, which leads to the equivalent pictures for the orthogonally-twisted monolayer/monolayer and bilayer/bilayer upon the rotations of the magnetic field by 90° ($\theta = 0^\circ$ vs $\theta = 90^\circ$). The differences between those idealized signals and an asymmetry in the experimental signal is attributed to the imperfection of the crystals and misalignment of the field/crystallographic axes.

For the antiferromagnet with easy-axis anisotropy character of the ground state's evolution under the variation of the magnetic field depends on the relative ratio between the anisotropy constant (*K*) and exchange constant between the two sublattices (*J*), both constants are given for the atomistic Hamiltonian. This phenomenon is described in ^[6]. In the case of bilayer of the CrSBr the two sublattices are formed by two layers. The phase diagram of the model Hamiltonian is depicted in the **Figure S19.b** where the magnetic field is swept from positive to negative values. Three phases are found to be possible: ferromagnetic phase: up or down (FPu and FPd), antiferromagnetic phase (AFP) and unconventional spin-flop phase, where spin is canted from the direction of the magnetic field and projection on the field direction is either up or down (SFPu and SFPd). All phases are schematically presented in the **Figure S19.b**. Three distinct cases are possible. First, the case of strong interlayer exchange ($K/J < 0.4$),

where the transition undergoes as FPu→SFPu→AFP→SFPd→FPd (red region in the figure). Characteristic chromium-based two-dimensional material for this scenario is CrPS₄, where the ratio between interlayer exchange and single-ion anisotropy is 0.028^[7] - 0.036^[8], that is well localized in the region of the case one. Indeed, phase transition with the intermediate spin-flop phase was observed experimentally for CrPS₄.^[9,10] Second, the case of the comparable interlayer exchange and magnetic anisotropy (0.4 < K/J < 1.2), where the transition has the order FPu→AFP→FPd, i.e. only one antiferromagnetic phase occurs. Experimental evidence for the CrSBr indicates that CrSBr falls into this case (green area in the figure).^[3] Finally, the third case with dominating anisotropy (K/J > 1.2), where the transition from FPu to FPd is happening directly.

Parametrisation of the effective micromagnetic parameters (in-layer and inter-layer exchange stiffness, anisotropy constants and saturation magnetisation) is based on the obtained atomistic model and further varied to fit the experimental results of the pristine bilayer. Atomistic single-ion anisotropy parameters are $K_a = 0.04 \text{ meV}$, $K_b = 0.08 \text{ meV}$ for medium (*a*) and easy (*b*) axis correspondingly. The anisotropic term of the Hamiltonian is written as

$$H_{aniso} = - \sum_i (K_a S_a^2 + K_b S_b^2)$$

where S_a and S_b are the projection of the classical spin vector on the direction of the medium and easy axis. Alternatively, if the following conventional Hamiltonian is used, i.e.

$$H_{aniso} = - \sum_i (D S_b^2 + E (S_a^2 - S_c^2))$$

then the parameters K_a and K_b can be expressed in terms of parameters D and E by the addition of an isotropic constant term. $K_a = 2E$, $K_b = D + E$, and $D = 0.06 \text{ meV}$, $E = 0.02 \text{ meV}$. Note the difference with $E' = 0 \text{ meV}$ and $D' = 0.0042 \text{ meV}$ or $D' = 0.0058 \text{ meV}$ previously reported for CrPS₄ (E' , D' are defined with respect to the out-of-plane easy axis of CrPS₄).^[7,8] Anisotropy parameters were taking from the atomistic picture and transformed into the micromagnetic one as (derived from the energy balance):

$$K_{u_1} = \frac{2KS^2}{abc}$$

where S^2 is a magnitude of the spin and a , b , c are the lattice parameters. Obtained values are provided in the **Table S2**.

On contrary, the interlayer exchange interactions predicted by DFT are usually small in CrSBr (of the order of 0.001 meV) and their reliability is an open question as those values are very sensitive to the used lattice parameters, exchange correlation pseudopotential choice and

inclusion of the Hubbard U and/or J correction. DFT is known to deliver a poor description of the interlayer van-der-Waals forces. In the case of CrSBr, our simulations predict an interlayer distance that is ~25 % larger than the experimental one. Thus, state-of-the-art DFT is expected to under-estimate inter-layer magnetic interactions in CrSBr. We have therefore decided to treat the micromagnetic interlayer exchange stiffness A_{ex}^{inter} as a free parameter in order to catch the behaviour of the CrSBr bilayer expected from the experiment. Namely, the appearance of only one antiferromagnetic phase under the sweep of the magnetic field with the symmetric (or close to symmetric) signal between the sweeps from positive to negative and negative to positive fields. Obtained micromagnetic interlayer exchange stiffness is presented in **Table S2**. Overall, our approach is the following: we compute the lattice structure parameters with $U=J=0$ to approximate the experimental values more closely (**Table S3**), and subsequently introduce the Hubbard correction $U-J$ to the electronic structure (including atomic force relaxation). With this procedure, the exchange parameters align more closely with those obtained from fittings to inelastic neutron scattering experiments.^[11] We explicitly avoid recalculating the lattice vectors with those $U-J$ values, as the vectors increase and deviate from the experimental value.

Finally, to match the experimentally observed values of the magnetic field for the phase transition on the bilayer we vary the saturation magnetisation M_{sat} . In-layer exchange stiffness is set to be approximately two orders of magnitude large than inter-layer exchange stiffness in order to ensure the ferromagnetic order inside each layer.

Then the same set of parameters is used to simulate monolayer/monolayer, bilayer/monolayer and for bilayer/bilayer the inter-layer exchange stiffness was doubled (see **Supporting Videos 4-7** for the values). As a first approximation the exchange stiffness between two pristine layers and between orthogonally-rotated layers is kept the same.

Table S2. Micromagnetic parameters used in the simulation for the pristine bilayer and each orthogonally-twisted heterostructure.

System	A_{ex}^{intra} , J/m	A_{ex}^{inter} , J/m	$K_{u_1}^a$, J/m ³	$K_{u_1}^b$, J/m ³	M_{sat} , A/m
bilayer	1.5×10^{-11}	-7.5×10^{-14}	1.9×10^5	3.8×10^5	1.0×10^6
monolayer/ monolayer	1.5×10^{-11}	-7.5×10^{-14}	1.9×10^5	3.8×10^5	1.0×10^6
monolayer/ bilayer	1.5×10^{-11}	-3.3×10^{-14}	1.9×10^5	3.8×10^5	1.0×10^6
bilayer/ bilayer	1.5×10^{-11}	-3.8×10^{-14}	1.9×10^5	3.8×10^5	1.0×10^6

Table S3: Lattice parameters of a CrSBr monolayer: experimental values and SIESTA calculations with several values of U (J=0 eV).

	Exp. ^[12]	U = 0 eV	U = 1 eV	U = 2 eV	U = 3 eV	U = 4 eV	U = 5 eV
a (Å)	3.50	3.59	3.61	3.63	3.65	3.67	3.69
b (Å)	4.74	4.82	4.86	4.90	4.93	4.96	4.99

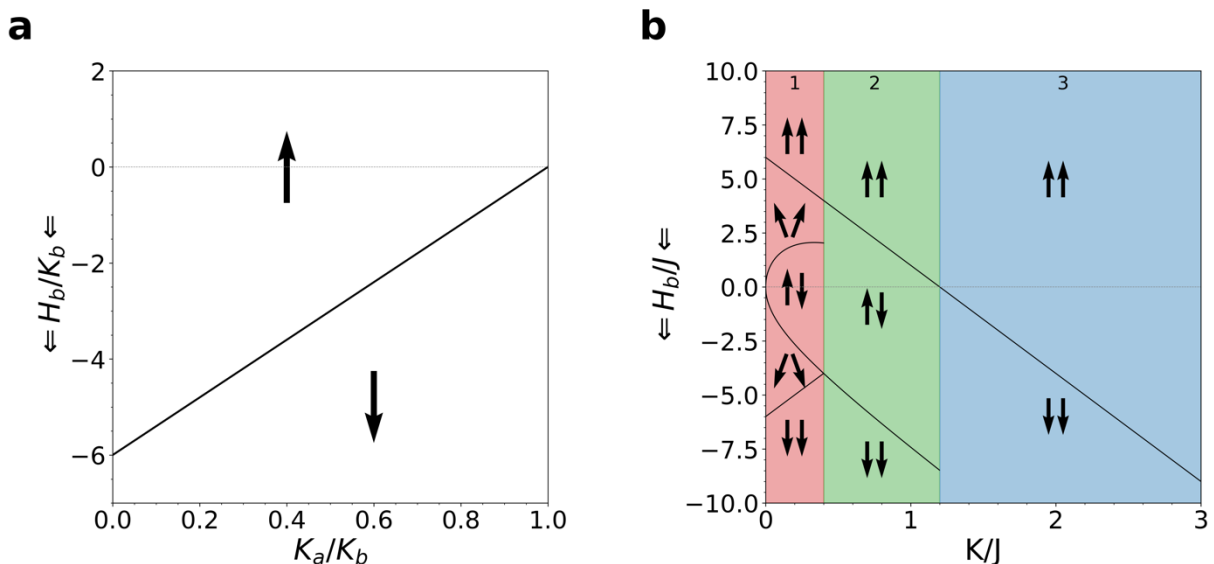


Figure S19.- Phase diagrams of pristine monolayer and pristine bilayer of CrSBr. a) Phase diagram of a pristine monolayer with the field applied along the easy-axis *b*. **b)** Phase diagram of the pristine bilayer with the field applied along the easy axis *b*. The direction of the magnetic field sweep is indicated in the y-axis label. The phase diagram has to be mirrored about the $y = 0$ line if the magnetic field is swept in reverse.

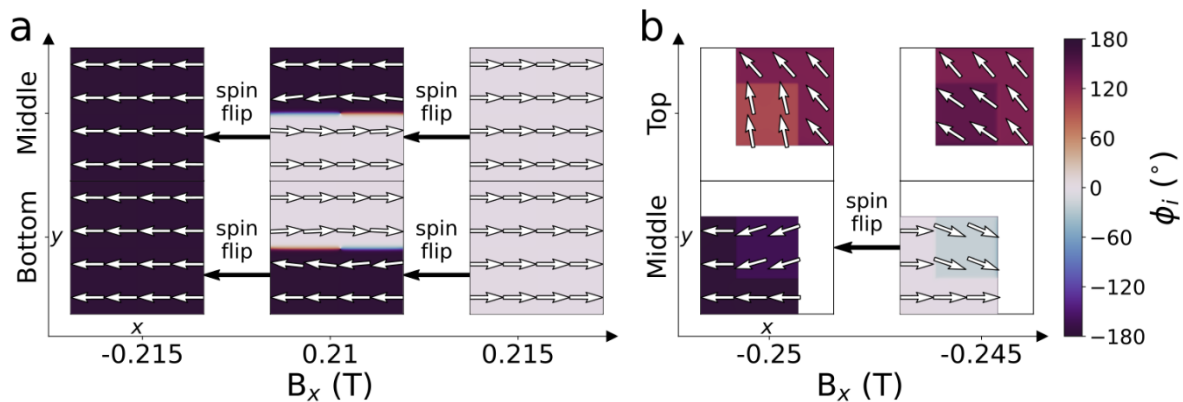


Figure S20.- Micromagnetic simulations of pristine bilayer and orthogonally-twisted bilayer (monolayer/monolayer system) CrSBr **a)** Snapshots of micromagnetic simulations for the pristine bilayer (**Supporting Video 4**), that correspond to the spin switches in **Figure 5e**. **b)** Snapshots of micromagnetic simulations for the monolayer/monolayer device (**Supporting Video 5**), that correspond to the spin switch marked in **Figure 5f**. Arrows indicate local direction of magnetisation in the xy -plane, colours indicate the angle ϕ_i measured from the x -direction for each layer.

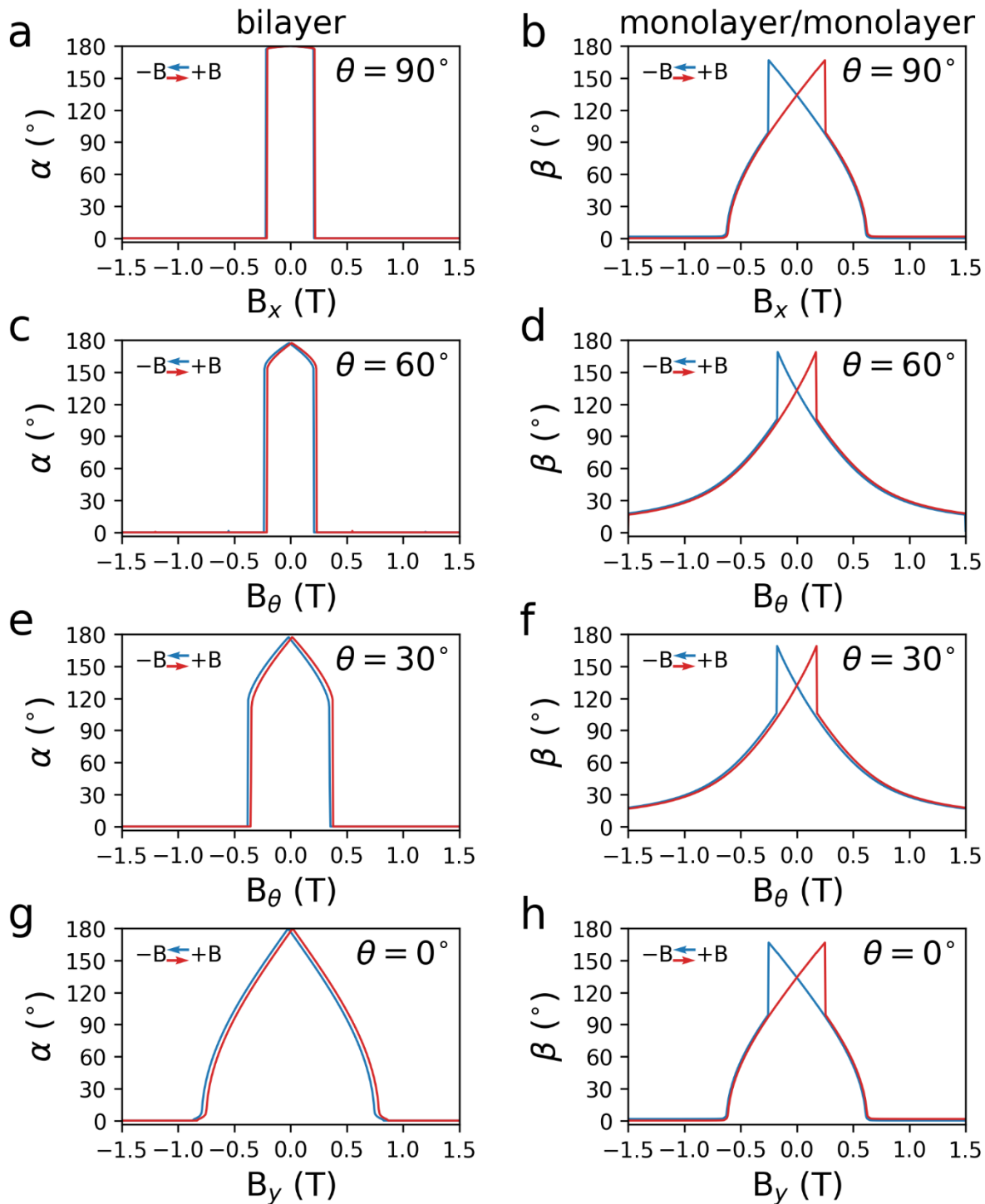


Figure S21.- Micromagnetic simulations for pristine bilayer and orthogonally-twisted monolayer/monolayer. a,c,e,g) Angles α between the neighbor layers for the pristine bilayer and (b,d,f,h) β for the orthogonally-twisted monolayer/monolayer. Magnetic field is applied along the four in-plane directions: (a-b) along the x axis; (c-d) with the angle of 30 degrees from x axis (or 60 degrees from y axis); (e-f) with the angle of 60 degrees from x axis (or 30 degrees from y axis); (g-h) along the y axis. Sweeps from left to right are mirrored sweeps from right to left and plotted for illustrative purposes. h) is plotted with the same data as b) due to the system symmetry (it is plotted for illustrative purposes only). d) and f) are simulated separately and confirm the symmetry of the system in simulations.

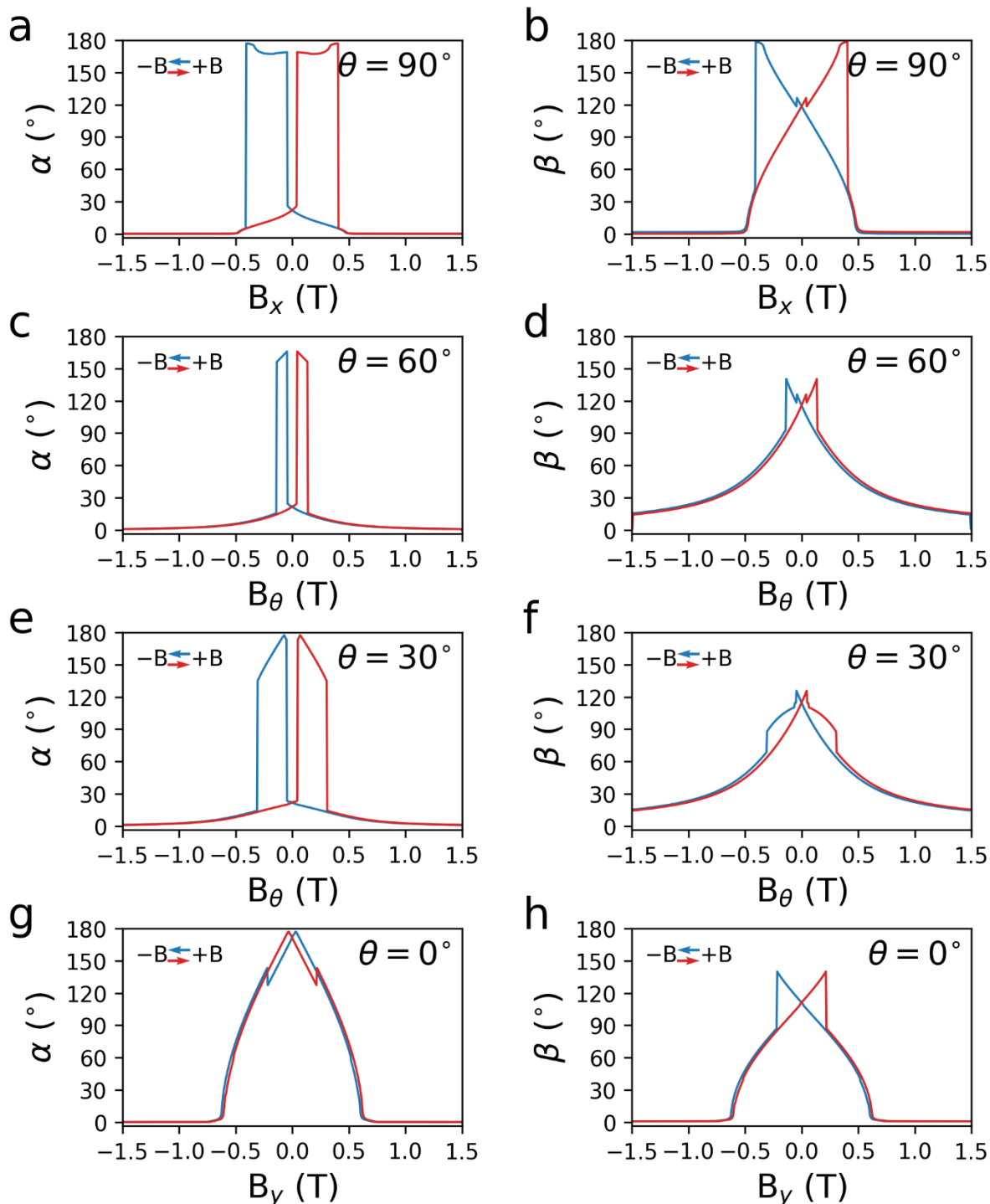


Figure S22.- Micromagnetic simulations for pristine bilayer and orthogonally-twisted bilayer/monolayer. Angles α (a,c,e,g) and β (b,d,f,h) as defined in the main text and **Figure 5b** between the neighbor layers for the orthogonally-twisted bilayer/monolayer. Magnetic field is applied along the four in-plane directions: (a-b) along the x axis; (c-d) with the angle of 30 degrees from x axis (or 60 degrees from y axis); (e-f) with the angle of 60 degrees from x axis (or 30 degrees from y axis); (g-h) along the y axis. Sweeps from left to right are mirrored sweeps from right to left and plotted for illustrative purposes.

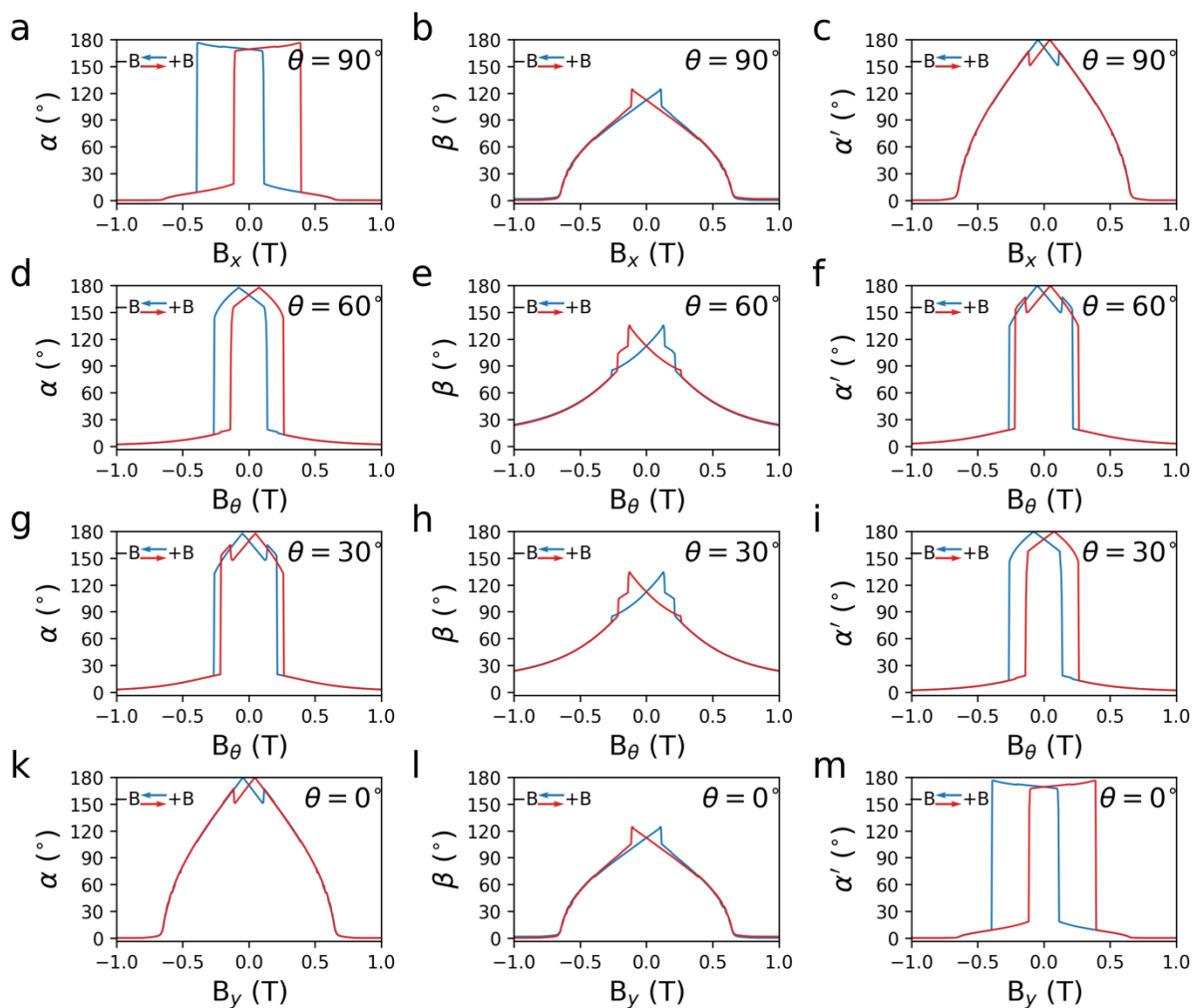


Figure S23.- Micromagnetic simulations for pristine bilayer and orthogonally-twisted bilayer/bilayer. a,d,g,k) Angles α (between non-twisted bottom and middle-bottom layers); b,e,h,l) Angles β (between orthogonally-twisted middle-bottom and middle-top layers); c,f,i,m) Angles α' (between non-twisted middle-top and top layers). Magnetic field is applied along the four in-plane directions: (a-c) along the x axis; (d-f) with the angle of 30 degrees from x axis (or 60 degrees from y axis); (g-i) with the angle of 60 degrees from x axis (or 30 degrees from y axis); (k-l,m) along the y axis. k,l,m) are plotted with the same data as c,b,a, correspondingly due to the symmetry of the system. d-i) are actually simulated separately and confirm the expected symmetry of the system. Sweeps from left to right are mirrored sweeps from right to left and plotted for illustrative purposes.

4.- Simplified model of the spin-switching process for orthogonally-twisted CrSBr.

This section illustrates the proposed spin-switching process for orthogonally-twisted monolayer/monolayer (**Figure S24**), monolayer/bilayer (**Figure S25**) and bilayer/bilayer (**Figure S26**) CrSBr. We consider sweeping the field from a negative saturated state to a positive saturated one. Reversing the field from positive to negative saturated states yields to the mirror image and is not illustrated for simplicity. The magnetic field is aligned along the easy-axis of one of the layers. At intermediate angles, where the field is not aligned to any easy-magnetic axis, the interpretation of the spin-switching mechanism is more complex, since it depends on a delicate interplay between the spin-flip and spin-reorientation of the layers with respect to the applied magnetic field (Zeeman energy), being the formation of spatial magnetic inhomogeneities —as magnetic domains— more likely, in line with the experimental observation of multistep transitions (**Figure 2**) and micromagnetic simulations (**Figure 5** and **Supporting Videos 4-7**).

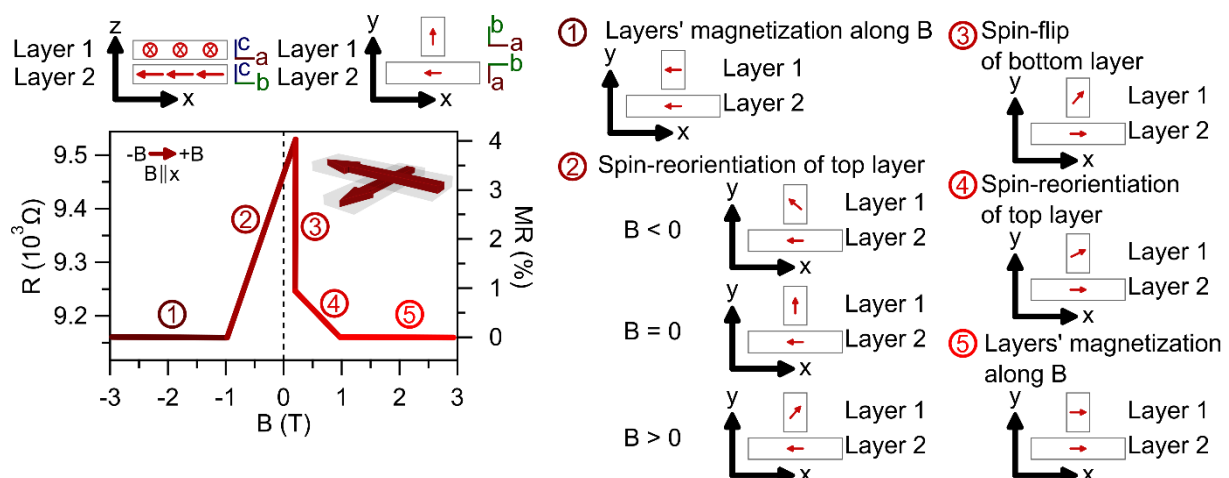


Figure S24.- Simplified model based on the spin-flip and spin-reorientation processes taken place in orthogonally-twisted monolayer/monolayer CrSBr.

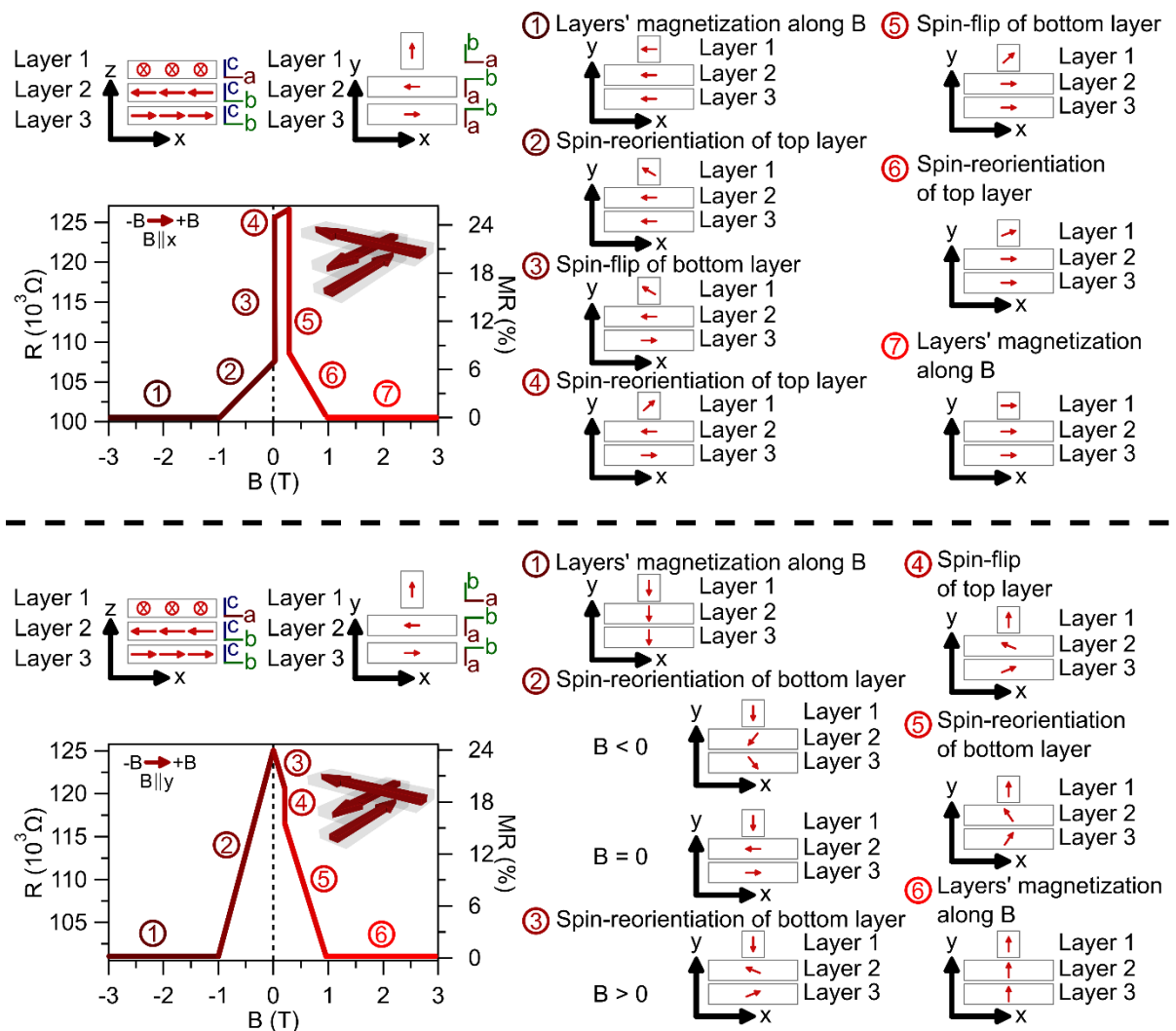


Figure S25.- Simplified model based on the spin-flip and spin-reorientation processes taken place in orthogonally-twisted monolayer/bilayer CrSBr.

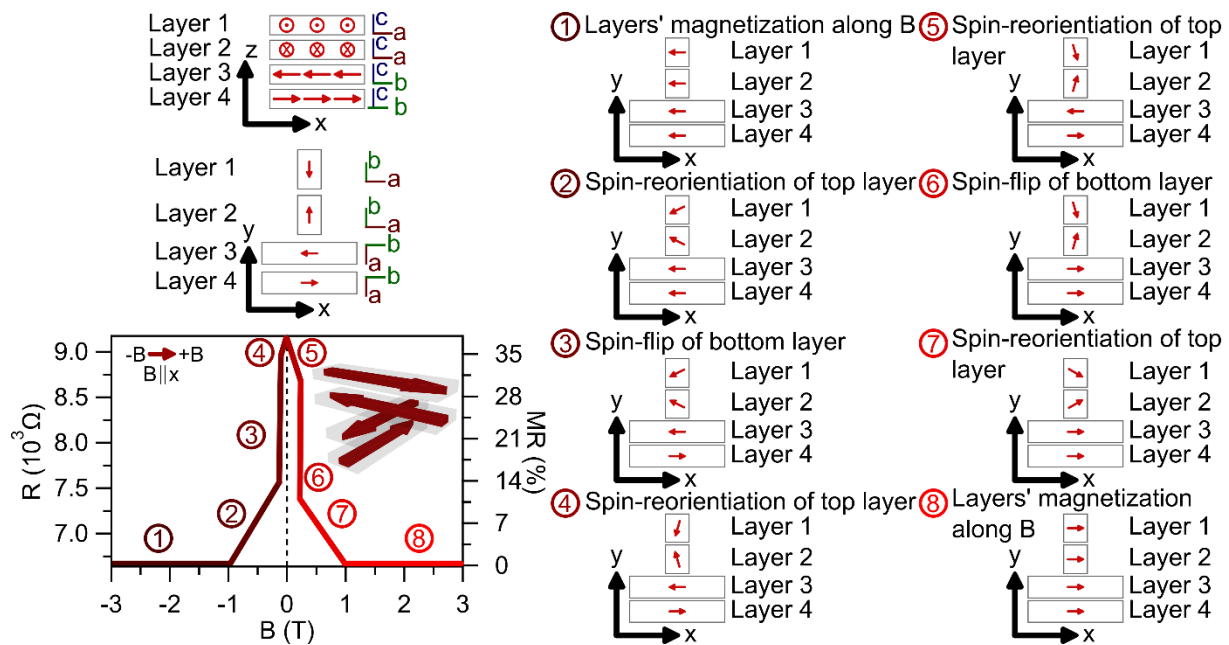


Figure S26.- Simplified model based on the spin-flip and spin-reorientation processes taken place in orthogonally-twisted bilayer/bilayer CrSBr.

5. References.

- [1] C. Boix-Constant, S. Jenkins, R. Rama-Eiroa, E. J. G. Santos, S. Mañas-Valero, E. Coronado, *Nat Mater* **2024**, *23*, 212.
- [2] E. J. Telford, A. H. Dismukes, R. L. Dudley, R. A. Wiscons, K. Lee, D. G. Chica, M. E. Ziebel, M.-G. Han, J. Yu, S. Shabani, A. Scheie, K. Watanabe, T. Taniguchi, D. Xiao, Y. Zhu, A. N. Pasupathy, C. Nuckolls, X. Zhu, C. R. Dean, X. Roy, *Nat Mater* **2022**, *21*, 754.
- [3] C. Boix-Constant, S. Mañas-Valero, A. M. Ruiz, A. Rybakov, K. A. Konieczny, S. Pillet, J. J. Baldoví, E. Coronado, *Advanced Materials* **2022**, *34*, 2204940.
- [4] G. Martínez-Carracedo, L. Oroszlány, A. García-Fuente, B. Nyári, L. Udvardi, L. Szunyogh, J. Ferrer, *Phys Rev B* **2023**, *108*, DOI 10.1103/PhysRevB.108.214418.
- [5] A. I. Liechtenstein, M. I. Katsnelson +, V. P. Antropov, V. A. Gubanov, *LOCAL SPIN DENSITY FUNCTIONAL APPROACH TO THE THEORY OF EXCHANGE INTERACTIONS IN FERROMAGNETIC METALS AND ALLOYS*, **1987**.
- [6] F. B. Anderson, H. B. Callen, *Physical Review* **1964**, *136*, A1068.
- [7] J. Son, S. Son, P. Park, M. Kim, Z. Tao, J. Oh, T. Lee, S. Lee, J. Kim, K. Zhang, K. Cho, T. Kamiyama, J. H. Lee, K. F. Mak, J. Shan, M. Kim, J. G. Park, J. Lee, *ACS Nano* **2021**, *15*, 16904.
- [8] S. Calder, A. V. Haglund, Y. Liu, D. M. Pajerowski, H. B. Cao, T. J. Williams, V. O. Garlea, D. Mandrus, *Phys Rev B* **2020**, *102*, DOI 10.1103/PhysRevB.102.024408.
- [9] Y. Peng, S. Ding, M. Cheng, Q. Hu, J. Yang, F. Wang, M. Xue, Z. Liu, Z. Lin, M. Avdeev, Y. Hou, W. Yang, Y. Zheng, J. Yang, *Advanced Materials* **2020**, *32*, DOI 10.1002/adma.202001200.
- [10] J. Y. Seo, S. Lim, H. J. Shin, K. W. Jeong, J. M. Hong, K. Moon, M. K. Kim, N. Lee, Y. J. Choi, *NPG Asia Mater* **2024**, *16*, DOI 10.1038/s41427-024-00559-3.
- [11] A. Scheie, M. Ziebel, D. G. Chica, Y. J. Bae, X. Wang, A. I. Kolesnikov, X. Zhu, X. Roy, *Advanced Science* **2022**, *2202467*, 2202467.
- [12] S. A. López-Paz, Z. Guguchia, V. Y. Pomjakushin, C. Witteveen, A. Cervellino, H. Luetkens, N. Casati, A. F. Morpurgo, F. O. von Rohr, *Nat Commun* **2022**, *13*, 4745.